Soil Dynamics and Earthquake Engineering 143 (2021) 106613

Contents lists available at ScienceDirect

Soil Dynamics and Earthquake Engineering

journal homepage: http://www.elsevier.com/locate/soildyn

Numerical modeling of soil liquefaction and lateral spreading using the SANISAND-Sf model in the LEAP experiments

Andrés Reyes [a], Ming Yang [a], Andrés R. Barrero [b], Mahdi Taiebat [a,*]

[a] Department of Civil Engineering, University of British Columbia, Vancouver, BC, Canada
[b] SRK Consulting (Canada) Inc., Vancouver, BC, Canada

ARTICLE INFO

Keywords:
Numerical modeling
Plasticity model
Cyclic liquefaction
Slope
Sand
Centrifuge tests

ABSTRACT

Laboratory element and centrifuge tests from LEAP-UCD-2017 and LEAP-Asia-2019 were used for model calibration and evaluation in a dynamic coupled analysis of a saturated and gently sloped deposit of sand subjected to base excitation. The paper focuses on using a recently proposed novel constitutive ingredient for modeling the post-liquefaction large cyclic shear strains in sands. An existing critical state compatible, bounding surface plasticity reference model is used, with and without this new constitutive ingredient, to explore its improved modeling capabilities. The constitutive model was first calibrated based on available laboratory element tests on Ottawa-F65 sand, and compared to the reference model showed significantly improved performance in capturing the strain-based liquefaction strength curve of a series of undrained hollow cylinder cyclic torsional shear tests. The calibrated models were used in Class-C prediction of the slope surface deformation in five centrifuge tests on a mildly sloping liquefiable ground of the same soil subjected to dynamic loading, in the three-dimensional finite difference program FLAC^{3D}. The simulation results were compared with experiments in terms of acceleration history, spectral response, excess pore water pressure development, and horizontal displacement evolution at specified control points. The vectors and contours of displacements at the end of shaking also revealed a pattern of slope deformation consistent with that of a gently sloped liquefiable ground. Following the insights from the performance of the models in simulation of the slope response, the calibration was adjusted to more realistically account for the impact of initial static shear stress on the development of post-liquefaction shear strains. The models were again used for Class-C1 prediction of the slope deformation of the same centrifuge tests. The overall assessment revealed the capabilities and limitations of the models in simulating the soil liquefaction strength and its post-liquefaction response.

1. Introduction

Performance-based analysis of soil deposits, when subjected to earthquake-induced shaking, is still a challenging task even in relatively simple configurations. Continuum mechanics-based numerical modeling platforms are the dominant means for carrying out such analyses, and among the key elements in these is the constitutive modeling of soils. There have been many advances in constitutive modeling of granular soils when subjected to cyclic shearing. Accounting for the shear-induced volumetric response, compliance with the critical state soil mechanics framework, and the role of inherent and loading induced anisotropies are some of the very useful constitutive features that have led to advancing the capabilities of soil models. Despite these advances, there are still many challenges to be addressed when dealing with the earthquake-induced liquefaction and post-liquefaction stress-strain response of soils. Addressing these challenges is especially important as performance-based analysis and design are becoming more common in geotechnical earthquake engineering practice.

Laboratory element tests play an essential role in understanding and characterizing the material response as they inspire the development of novel constitutive features, which can, in turn, be validated by the related established databases. Successful simulation of these element tests provides a certain level of confidence and promise for more reliable simulation of boundary value problems (BVPs), which is the ultimate goal of such models. Physical simulation of BVPs, when carefully conducted, provides valuable data for evaluation and validation of numerical modeling methods including, but not limited to, the role of the material constitutive model and its range of applicability and

* Corresponding author.
E-mail addresses: reyespa@mail.ubc.ca (A. Reyes), yangm15@civil.ubc.ca (M. Yang), abarrero@srk.com (A.R. Barrero), mtaiebat@civil.ubc.ca (M. Taiebat).

https://doi.org/10.1016/j.soildyn.2021.106613
Received 17 December 2019; Received in revised form 14 December 2020; Accepted 20 December 2020
Available online 13 February 2021

limitations. For geotechnical problems, centrifuge tests are particularly of interest and importance in providing insights into the response of soil system BVPs. These tests have evolved and improved over the years and, when carefully conducted, can lead to useful data for specific problems related to soil response in various modes of loading, including the dynamic excitations.

A recent collaborative international liquefaction benchmark study, named Liquefaction Experiments and Analysis Projects (LEAP), has been built upon the pioneering work of the Verification of Liquefaction Analyses and Centrifuge Studies (VELACS) [1], and aims specifically at the combined use of advanced centrifuge testing and numerical modeling as described in Manzari et al. [2]. LEAP has produced and continues to produce a wealth of physical testing data to investigate the challenges related to the liquefaction and post-liquefaction of soils. Since its inception, three projects have been organized within LEAP: LEAP-GWU-2015 [3], LEAP-UCD-2017 [4], and LEAP-Asia-2019 [5]. The theme in these three projects has been on the liquefaction and lateral spreading of a mildly sloping submerged medium dense, clean sand deposit, subjected to base excitation; each series has focused on different specific objectives. LEAP-GWU-2015 was the first in this series with 6 centrifuges tests on uniform medium dense sand with a 5-degree slope in a rigid container subject to a ramped, 1 Hz sine wave base motion. LEAP-UCD-2017 focused on repeatability and sensitivity of the response to variation of density and base motion intensity. LEAP-Asia-2019 focused on the validation of generalized scaling law of Iai et al. [6]. The authors participated in the numerical simulation part of the latter two projects, and their corresponding simulation results have been summarized in Yang et al. [7] and Reyes et al. [8], respectively.

The main objective of this study is to present the application of a new model, named SANISAND-Sf, to the simulation of shaking-induced liquefaction and the resulting lateral displacements of a gentle slope. The numerical simulations are evaluated against physical modeling and, more specifically, selected centrifuge tests performed as part of the LEAP project. The formulation of the SANISAND-Sf model is an extension of the basic SANISAND framework (Dafalias and Manzari, 2004 [9]), or DM04, intending to overcome the inability of the DM04 model to simulate accurately post-liquefaction shear strain development. It was shown in a recent work by the authors [10] that the proposed extension accomplished its mission when tested against some element tests. As the next step, the objective of this work is to evaluate the proposed extension in boundary value modeling.

In Section 2, the constitutive model is briefly introduced with a focus on the role of the newly proposed constitutive ingredient in modeling the post-liquefaction large cyclic shear strains, along with its calibration and selected results of the performance of the reference and extended models based on the LEAP laboratory element tests on Ottawa-F65 sand. Section 3 presents the key aspects of the five selected LEAP centrifuges tests and the corresponding numerical models used for their simulation. Class-C simulation results of the centrifuge experiments, using both the reference model and the extended model, are presented and discussed in Section 4. With a focus on the importance of accounting for initial static shear stresses in modeling the cyclic shear strains, additional Class-C1 simulations were carried out, and the resulting surface lateral displacements were examined. Finally, sensitivity analyses illustrated the effects of sand relative density and input ground motion on the slope's simulated response. Conclusions from this study are presented in Section 5.

2. Constitutive model

The constitutive model used in the present study follows the basic premises of the original two-surface plasticity model of Manzari and Dafalias [11] and revised by Dafalias and Manzari in 2004 [9], which formed the basis of what was later on named SANISAND class of models [12]. The SANISAND models follow the framework of bounding surface plasticity with kinematic hardening of yield surface and critical state soil mechanics concepts, allowing a unified description of any pressure and density by the same set of model constants. The Dafalias and Manzari 2004 model [9], abbreviated as DM04 in this paper, represents the core of the constitutive model, and various subsequent works include the extensions of the SANISAND class [12–17], building into it different constitutive features that can be added to the original framework.

The DM04 model is well established for constitutive modeling of monotonic and cyclic response of sands in the pre-liquefaction stage, and has been widely used over the years [18–21]. Despite its success in modeling specific aspects of soil liquefaction, the DM04 and all above members of the SANISAND family of models have a major limitation in capturing the post-liquefaction cyclic shear strain development of sands. Experimental data of LEAP-UCD-2017 and LEAP-Asia-2019 projects has led to addressing the constitutive modeling of this complex issue. For this purpose, Barrero et al. [10] introduced a new constitutive ingredient reflecting the physical existence of a "semifluidized (Sf) state" for very low effective mean stress reached in the post-liquefaction stage. It introduced a new internal degradation variable for plastic modulus and dilatancy, that increases towards a saturation value of unity during undrained cyclic loading, while it demises in a continuous way upon subsequent drainage. The increase of this internal variable and its influence on the plastic modulus and dilatancy is active only for states within the Sf state while leaving almost intact the response outside of it.

The proposed formulation is then incorporated into the DM04 model, and the new model is referred to as SANISAND-Sf [10] because it belongs to the SANISAND family of models and includes the new constitutive notion of Sf state. This section summarizes the key additions of the SANISAND-Sf model, used in this study, to the reference DM04 model.

Table 1
SANISAND-Sf model equations and associated constants.

Description	SANISAND-Sf equations	Constants[a]
Elastic relations	$\dot{\varepsilon}_v^e = \dot{p}/K;\quad \dot{\mathbf{e}}^e = \dot{\mathbf{s}}/(2G)$	
Plastic relations	$\dot{\varepsilon}_v^p = \langle L\rangle D;\quad \dot{\mathbf{e}}^p = \langle L\rangle \mathbf{R}'$	
Hypoelastic moduli	$G = G_0 p_{at}(2.97-e)^2/(1+e)(p/p_{at})^{1/2}$	G_0
	$K = 2(1+\nu)G/[3(1-2\nu)]$	ν
Critical state line	$M = g(c,\theta)M^c$	M^c, c
	$e_c = e_c^{ref} - \lambda_c(p/p_{at})^{\xi}$	e_c^{ref}, λ_c, ξ
Yield surface	$f = \sqrt{(\mathbf{s}-p\boldsymbol{\alpha}):(\mathbf{s}-p\boldsymbol{\alpha})} - \sqrt{2/3}pm = 0$	m
Kinematic hardening	$\dot{\boldsymbol{\alpha}} = \langle L\rangle (2/3)h(\boldsymbol{\alpha}_\theta^b - \boldsymbol{\alpha})$	
	$\boldsymbol{\alpha}_\theta^b = \sqrt{2/3}[M\exp(-n^b\psi) - m]\mathbf{n}$	n^b
	$h = b_0/[(\boldsymbol{\alpha}-\boldsymbol{\alpha}_{in}):\mathbf{n}]$	
	$b_0 = G_0 h_0 (1 - c_h e)(p/p_{at})^{-1/2}$	c_h
	$h_0 = h_0'\Lambda$	h_0'
Deviatoric flow rule	$\mathbf{R}' = B\mathbf{n} - C[\mathbf{n}^2 - (1/3)\mathbf{I}]$	
	$\mathbf{n} = (\mathbf{r}-\boldsymbol{\alpha})/\|\mathbf{r}-\boldsymbol{\alpha}\|$	
	$B = 1 + 3(1-c)/(2c)g(\theta,c)\cos 3\theta$	
	$C = 3\sqrt{3/2}(1-c)g(\theta,c)/c$	
	$g(\theta,c) = 2c/[(1+c) - (1-c)\cos 3\theta]$	
Dilatancy	$D = A_0(1 + \langle \mathbf{z}:\mathbf{n}\rangle)(\boldsymbol{\alpha}_\theta^d - \boldsymbol{\alpha}):\mathbf{n}$	
	$A_0 = A_0'\Lambda$	A_0'
	$\boldsymbol{\alpha}_\theta^d = \sqrt{2/3}[M\exp(n^d\psi) - m]\mathbf{n}$	n^d
	$\dot{\mathbf{z}} = -c_z\langle -\dot{\varepsilon}_v^p\rangle(z_{max}\mathbf{n} + \mathbf{z})$	c_z, z_{max}
Semifluidized state	$p_r = p/p_{th}$	$p_{th} = 10$ kPa
	$\Lambda = [(1-\langle 1-p_r\rangle)^{x\ell} + f_\ell]$	x, $f_\ell = 0.01$
	$\dot{\ell} = \langle L\rangle[(p_{in}/p_{inr})^a c_\ell\langle 1-p_r\rangle(1-\ell)^{n_\ell}] - c_r\ell\lvert\dot{\varepsilon}_v\rvert$	c_ℓ, p_{inr}, a, $n_\ell = 8$, c_r

[a] Some constants have indicated default numerical values.

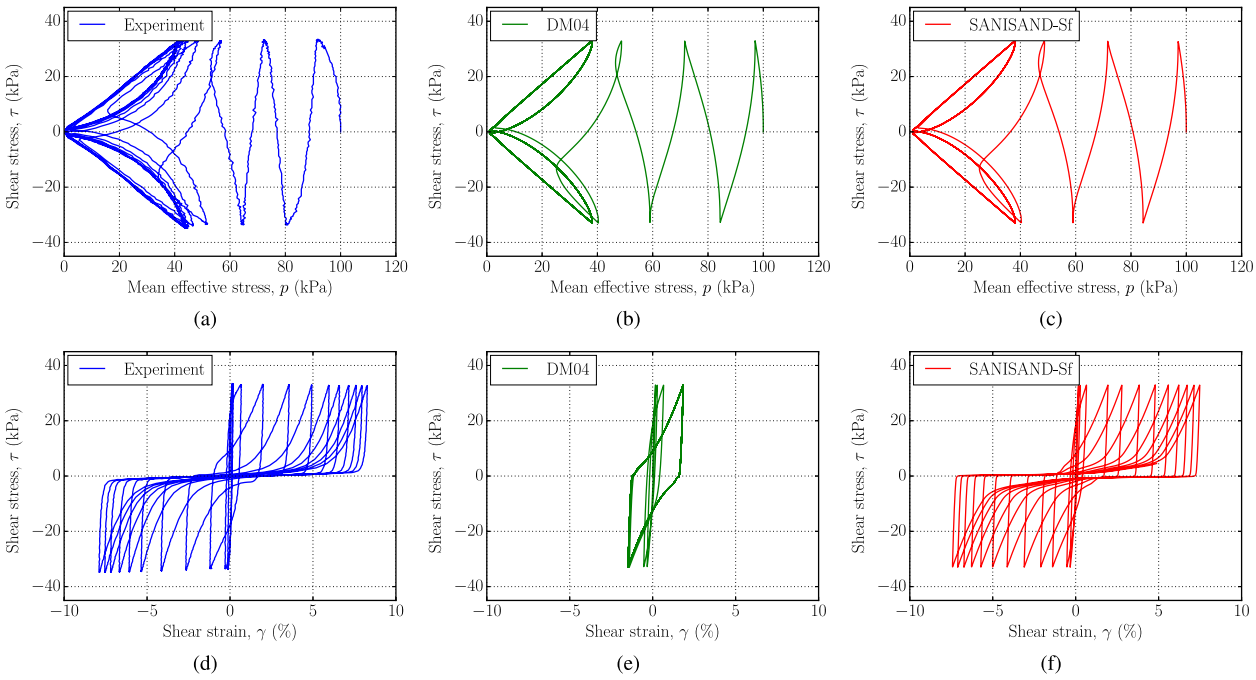

Fig. 1. Simulations compared with experiments in undrained hollow cylinder cyclic torsional shear test with CSR = 0.33 on isotropically consolidated sample of Toyoura sand with $D_r = 70\%$: (a), (d) experimental data from Zhang [22]; (b), (c)simulations using DM04; (c), (f) simulations using SANISAND-Sf.

2.1. SANISAND-Sf

The constitutive equations of the SANISAND-Sf model are summarized in Table 1. More details on the reference DM04 model are provided in the related reference [9] and not repeated here for brevity. However, the novel ingredient of strain liquefaction factor related to the semifluidized state, as well as the resulting key revisions on the reference model, are included here so that the reader can more easily follow related discussions.

The necessity of introducing this new constitutive ingredient arose from observing that the stress-strain loops of the DM04 model in the post-liquefaction stage appear to lock-up within a few cycles, preventing

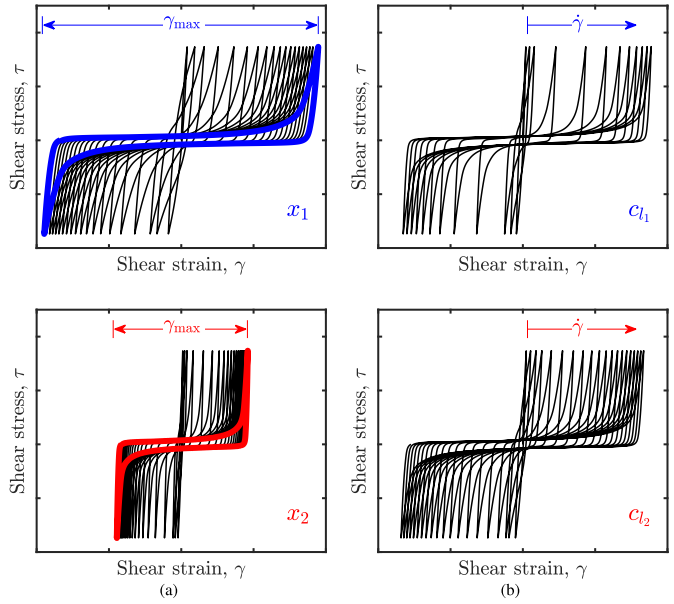

Fig. 2. Schematic illustration of the roles of the primary model constants linked to Sf state in SANISAND-Sf model for a single CSR level: (a) x controls the γ_{max}, where $x_1 > x_2$; and (b) c_ℓ defines the pace of development of γ as well as the number of cycles in the post-liquefaction stage, where $c_{l_1} > c_{l_2}$.

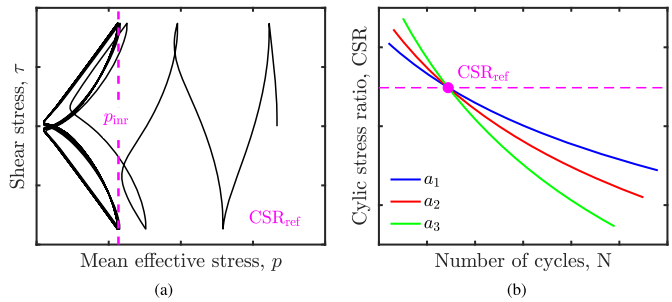

Fig. 3. Schematic illustration of the roles of the primary model constants linked to Sf state in SANISAND-Sf model for a range of CSR levels: constant a controlling the *slope* of the strain-based cyclic resistance curve along with reference to the interrelated constants CSR_{ref} and p_{inr}. In the figure $a_1 > a_2 > a_3$.

the model from capturing the increase of cyclic shear strains amplitude with the number of cycles as seen in the experiments. An example of this problem is illustrated in Fig. 1. In particular, Fig. 1(a) and (d) show experimental data from Zhang [22] on the stress path and stress-strain of an undrained hollow cylinder cyclic torsional shear test on Toyoura sand under a cyclic stress ratio CSR = 0.33. Here CSR is the ratio of cyclic shear stress amplitude τ^{amp} and the initial mean effective stress p_0. While the experimental data shows progressive increase of the cyclic shear strain amplitude in the post-liquefaction stage, the corresponding simulation using DM04 in Fig. 1(b) and (e) shows locking of the stress-strain loops in the post-liquefaction stage. Fig. 1(c) and (f) show the superior performance of the new SANISAND-Sf model compared to the reference DM04 model in capturing the accumulation of cyclic shear strain in the post-liquefaction stage. More details about the details of the adopted novel constitutive ingredient and the calibration process are presented in the remainder of this section.

Inspired by observations from laboratory element tests and numerical discrete element simulations of undrained cyclic shear tests on granular materials [23–25], the concept of Sf state was introduced, which refers to the state of granular material when the mean effective stress is very small, namely when $p < p_{th}$ with the threshold mean effective stress p_{th} being a model constant with the default value 10 kPa. An internal state variable named Strain Liquefaction Factor (SLF) and symbolized by ℓ is introduced, whose purpose is to reduce stiffness and dilatancy only within the Sf state, by decreasing the values of h_0 and A_0 listed in Table 1, according to the two following equations:

$$h_0 = h_0^{'}[(1 - \langle 1 - p_r \rangle)^{x\ell} + f_\ell] \tag{1}$$

$$A_0 = A_0^{'}[(1 - \langle 1 - p_r \rangle)^{x\ell} + f_\ell] \tag{2}$$

where x and f_ℓ are model constants, the latter with the default value 0.01. The pressure ratio $p_r = p/p_{th}$ compared to 1 determines if the stress falls into the Sf state. Note that $1 - p_r$ is enclosed into Macaulay brackets representing a ramp function, i.e., $\langle 1 - p_r \rangle = 1 - p_r$ if $p_r < 1$ and $\langle 1 - p_r \rangle = 0$ if $p_r \geq 1$. The common factor appearing in Eqs. (1) and (2) is represented by Λ in Tables 1 and i.e., $\Lambda = [(1 - \langle 1 - p_r \rangle)^{x\ell} + f_\ell]$. The primed quantities $h_0^{'}$ and $A_0^{'}$ are, in fact, the model constants h_0 and A_0 of DM04, respectively. The new h_0 will transfer via b_0 the effect of ℓ on the value of h, which eventually affects the plastic modulus K_p, as listed in Table 1. Observe that outside Sf state one has $p_r > 1$, hence, $\Lambda = 1 + f_\ell$ or $h_0 = h_0^{'}(1 + f_\ell)$ and $A_0 = A_0^{'}(1 + f_\ell)$, where given the very small value of $f_\ell = 0.01$, the h_0 and A_0 recover their original values. Therefore, the model response is not altered when the stress is outside the Sf state. The common factor Λ multiplying $h_0^{'}$ and $A_0^{'}$ implies that $h_0^{'}/A_0^{'} = h_0/A_0$, and since the rate of plastic volumetric strain is proportional to D/K_p, it follows that within the Sf state this rate is unaltered by the modifications of $h_0^{'}$ and $A_0^{'}$ to h_0 and A_0, respectively.

The ℓ evolves only when $p < p_{th}$ or $p_r < 1$ according to:

$$\dot{\ell} = \langle L \rangle \left[\left(\frac{p_{in}}{p_{inr}} \right)^a c_\ell \langle 1 - p_r \rangle (1 - \ell)^{n_\ell} \right] - c_r \ell \left| \dot{\varepsilon}_v \right| \tag{3}$$

where c_ℓ, n_ℓ, p_{inr}, a, and c_ℓ are new model constants, with a default value $n_\ell = 8$. The constant c_r in the last term of Eq. (3), is responsible for controlling the pace of the demise of ℓ towards zero when drainage or reconsolidation occurs, and is meant for successful simulation of multiple-liquefaction stages. In the absence of such data for calibration of this constant, this feature is deactivated by setting $c_r = 0$ in the present study.

The primary model constants linked to Sf state and to be calibrated consist of c_ℓ, p_{inr}, and a entering Eq. (3) for the evolution of ℓ, and x entering Eqs. (1) and (2) and controlling how much the SLF ℓ affects the plastic modulus and dilatancy. The effects of each model constant on the stress-strain loops in post-liquefaction stage and liquefaction strength curve are illustrated in Figs. 2 and 3.

It should be noted that one underlying assumption in SANISAND-Sf is that the cyclic shear strain amplitude cannot develop unboundedly: at the max value of $\ell = 1$, the stress-strain loops get stuck at a maximum cyclic shear strain amplitude γ^{max}. Although laboratory observations have not thoroughly verified this assumption, several discrete element simulations [23,24] suggest that stress-strain loops do saturate in the post-liquefaction stage. As shown qualitatively in Fig. 2(a), the simulated γ^{max} can be controlled by tuning the value of x. If the experiments do not show an apparent value of γ^{max}, as is the case for many of the laboratory element tests, one can vary x to capture the general trend of shear strain development. Then, c_ℓ should be tuned to appropriately capture the pace of evolution of cyclic shear strain amplitude towards γ^{max}, as illustrated qualitatively in Fig. 2(b).

The constants p_{inr} and a are introduced specifically for controlling the model performance in the post-liquefaction stage at different levels of CSR. Most notably, these two inter-related constants are to capture the strain-based liquefaction strength curve. In an undrained cyclic shear loading with a CSR_{ref}, the p_{inr} is the mean stress at the reversal points of the stress path in the "locked" butterfly shape of subsequent contraction and dilation phases, as shown in Fig. 3(a). Based on this p_{inr}, the constant a will influence the $\dot{\ell}$ in other levels of CSR, hence the number of cycles for reaching a certain level of shear strain amplitude. In other words, the pair of p_{inr} and a can control the strain-based liquefaction strength curve, as shown in Fig. 3(b). The calibration procedure of the constants related to the Sf state is therefore quite simple: (i) With an aleatory value of a and for the test associated to CSR_{ref}, one can simulate its stress-strain response by tuning x and c_ℓ to attain a good match with the experiment, hence the reference point in Fig. 3(b); (ii) the value of a should then be tuned to match the desired slope of the liquefaction strength curve, as also illustrated in Fig. 3(b). Consequently, it is of importance to select a representative reference experiment for

Table 2
SANISAND-Sf calibrated model constants for Ottawa-F65 sand.

Description	Symbol	Class-C	Class-C1
Elasticity	G_0	125	125
	ν	0.05	0.05
Critical state	M^c	1.26	1.26
	c	0.8	0.8
	e_c^{ref}	0.78	0.78
	λ_c	0.0287	0.0287
	ξ	0.8	0.8
Yield surface	m	0.02	0.02
Kinematic hardening	n^b	2.3	3.5
	h_0'	6	8
	c_h	0.968	0.968
Dilatancy	n^d	2.5	2.5
	A_0'	0.5	0.5
	z_{max}	25	15
	c_z	2000	2000
Semifluidized state	x	3	4
	c_ℓ	80.0	90.0
	p_{inr}	18 kPa	18 kPa
	a	8	8
	c_r	0[a]	0[a]

[a] Calibration requires data for multiple-liquefaction stages.

calibration, CSR_{ref}, as the model response for other amplitudes of cyclic shear stress depends on it. Furthermore, one must be mindful that while the overall fitting of the CSR-N curve is satisfactory, this is often achieved by balancing the under and overprediction of N in the pre- and post-Sf range, respectively. The ideal scenario would be to have separate satisfactory simulations of the CSR-N curves for these two ranges; this is a subject of an ongoing investigation.

The SANISAND-Sf model has been numerically implemented as a user-defined material model in the finite difference program FLAC^{3D} [26] using the cutting-plane algorithm, including a pressure-dependent sub-stepping, as the stress integration scheme. The implementation includes additional numerical treatments to efficiently handle low mean stresses and the mixed-discretization approach of the adopted numerical platform [27]. The user-defined material model is then compiled in the form of a dynamic link library (DLL) for FLAC^{3D} . The resulting DLL file is used for simulating the element level and boundary value problems such as the one in the present study.

2.2. Simulation of element level tests

In preparation for simulating the centrifuge experiments, the SANISAND-Sf model was calibrated against a series of laboratory element tests on the designated Ottawa-F65 sand for LEAP-UCD-2017 and LEAP-Asia-2019. In particular, the reference database for LEAP-UCD-2017 included two sets of element tests on the Ottawa F-65 sand: monotonic and cyclic triaxial tests by Vasko [28], and monotonic and cyclic simple shear tests by Bastidas [29]. The material characterization in LEAP-Asia-2019 included supplementary stress-controlled undrained hollow cylinder cyclic torsional shear tests, as reported in Vargas et al. [30].

Aside from the constants with default numerical values, SANISAND-Sf model requires the calibration of 20 model constants: 15 inherited from DM04, and the remaining 5 related to the Sf state. Details of the calibration process for DM04 model constants have been elaborated in earlier works [e.g., 8, 17]. As stated before, the constant c_r of the SANISAND-Sf was set to 0 in this work. The remaining four new model constants were calibrated following the procedure outlined in the previous section. In calibration of the SANISAND-Sf model for Ottawa-F65 sand, most of the model constants of DM04 were adopted from Yang et al. [7] and then the model constants including c, n^b, n^d, A_0, h_0, c_z and z_{max} were adjusted to better capture the stress path of the undrained hollow cylinder cyclic torsional shear tests of Vargas et al. [30].

In this first phase, the calibration of model constants only focused on capturing the soil behavior at an element level, with no reference to the centrifuge experimental results. This calibration is considered as Class-C according to the classification proposed by Lambe [31], as these constants were then used in prediction of response in slope boundary value problems modeled in the centrifuge. The calibrated model constants in this phase are listed in Table 2 under the category of Class-C.

Fig. 4 presents comparisons between the experimental data and both DM04 and SANISAND-Sf simulation results for a selected undrained hollow cylinder cyclic torsional shear test with CSR = 0.20 on an isotropically consolidated sample of Ottawa-F65 sand with D_r = 60%. The results are presented in terms of stress path, stress-strain loops, excess pore water pressure generation, and shear strain development. The reference DM04 simulation was carried out by deactivating the Sf state part of the SANISAND-Sf model. One can observe that both simulations match the experiment well in the pre-liquefaction stage in terms of stress paths shown in Fig. 4(a), (b) and (c), and the associated pore water pressure accumulation in Fig. 4(g), except for the first quarter of loading cycle where the model simulates a smaller generation of excess pore pressure. Comparisons of the shear-strain loops in Fig. 4(d), (e), and (f) along with shear strain development in Fig. 4(h) reveal the possibility of capturing the increase of strain amplitudes in the post-liquefaction stage using the novel feature of Sf state. More specifically, while the stress-strain loops of DM04 are locked-up in the post-liquefaction stage, SANISAND-Sf manages to progressively develop shear strain, showing more comparable performance with the experiment. The only exception is that in the first liquefaction cycle, there is a sudden development of shear strains in the simulation, while the trend is more gradual in the experiment.

The overall performance of the SANISAND-Sf in simulating the nine available undrained hollow cylinder cyclic torsional shear tests [30] with relative densities D_r = 50% and 60% is summarized in capturing the liquefaction strength curve, namely, CSR versus the number of loading cycles to initial liquefaction, as shown in Fig. 5. Here, the criterion for initial liquefaction is chosen as reaching 7.5% "double amplitude" of cyclic shear strain, i.e., γ_{DA} = 7.5%. It should be noted that such strain-based liquefaction strength curve is not even achievable using the DM04 model neither in cyclic torsional test nor in cyclic triaxial test; this is because of the known problem related to the locking of the stress-strain loops in the post-liquefaction stage previously illustrated in Fig. 4(e). The SANISAND-Sf calibrated model constants appear to show a satisfactory simulation of these strain-based liquefaction resistance curves, with slightly better performance for the tests with D_r = 60%, and medium to high levels of CSR. Further inspection of detailed stress-path and stress-strain loops (not shown here) revealed better performance at higher CSR levels for both levels of D_r. It is relevant to mention that the selected centrifuge tests consisted of sand deposits with relative densities around 60%. Furthermore, they were subjected to intense enough shaking to cause extensive soil liquefaction, which can relate to element tests at high levels of CSR. Hence, this set of calibrated model constants was expected to be reasonable for the target BVPs.

3. Physical and numerical models

Five centrifuge tests, including two from LEAP-UCD-2017 and three from LEAP-Asia-2019, were selected in this study as the boundary value problems of interest. The experimental results of all these tests showed evidence of experiencing liquefaction during the base excitation process. A description of these centrifuge tests, the adopted numerical platform for the simulations, the set up the numerical model, and details of the simulation procedure are presented in this section.

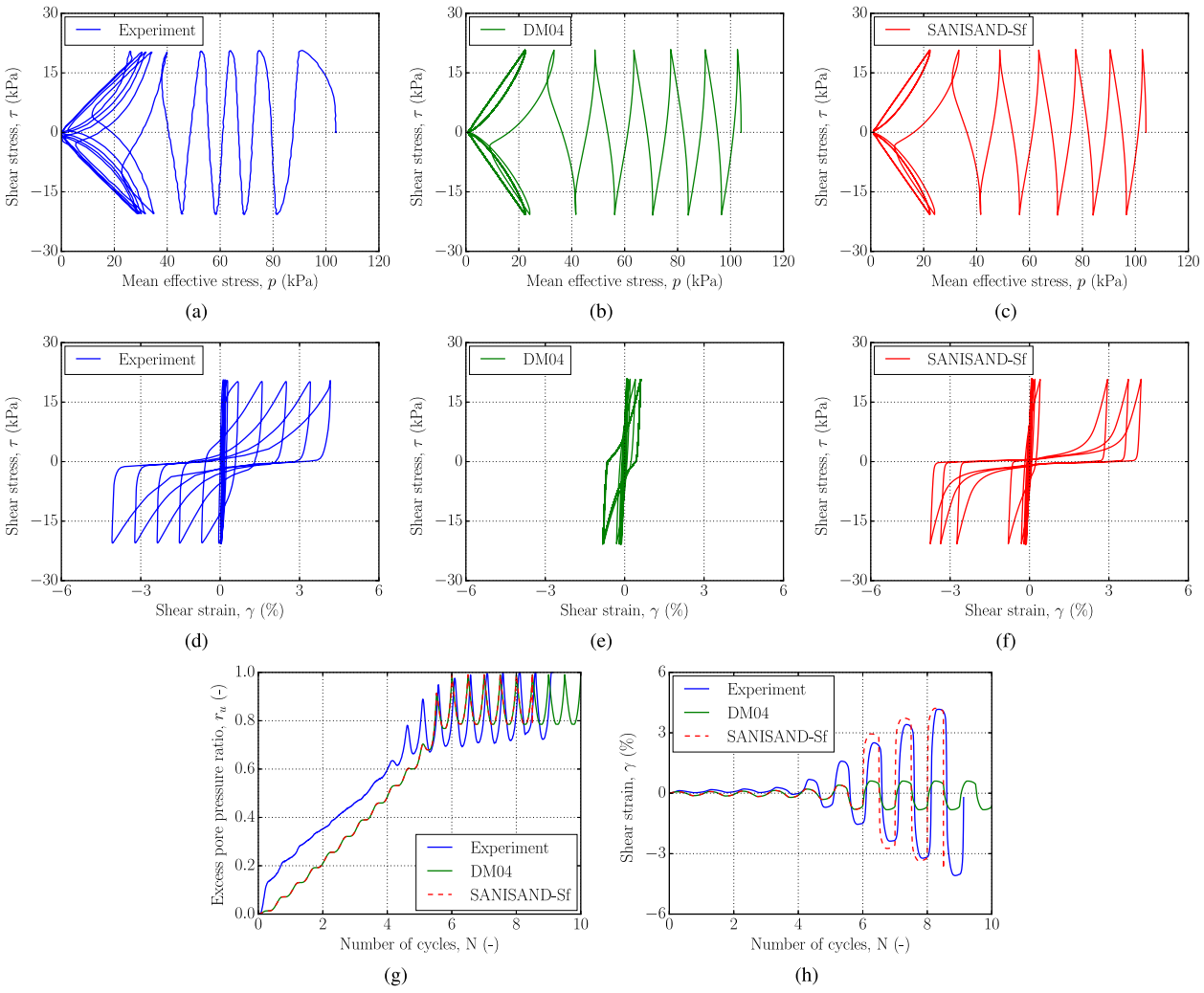

Fig. 4. Simulations compared with experiment in undrained hollow cylinder cyclic torsional shear tests with CSR = 0.20 on isotropically consolidated sample of Ottawa-F65 sand with D_r = 60%: (a), (d) experimental data from Vargas et al. [30]; (b), (e) simulations using DM04; (c), (f) Class-C simulations using SANISAND-Sf; (g), (h) comparisons between experiment and simulations of DM04 and SANISAND-Sf in terms of pore water pressure generation and shear strain development.

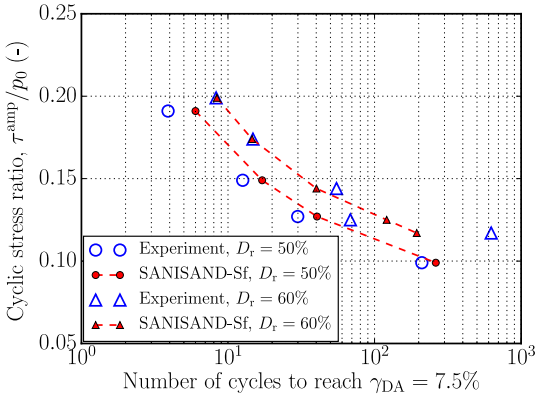

Fig. 5. Experimentally measured and SANISAND-Sf simulated (Class-C) liquefaction strength curves to reach γ_{DA} = 7.5% for Ottawa-F65 sand with D_r = 50% and 60%. The corresponding curves from DM04 simulations are not presented here as it did not reach the γ_{DA} = 7.5% criterion at these CSR levels.

Table 3
Basic properties of Ottawa F-65 sand [4].

Property	Range	Recommended value
Maximum density (kg/m^3)	1732–1793	1757
Minimum density (kg/m^3)	1432–1538	1491
Specific gravity, G_s	2.58–2.68	2.65
Hydraulic conductivity (cm/s)	0.010–0.016	0.0207 $\times e-$ 0.0009[a]

[a] e refers to void ratio.

3.1. Description of centrifuge tests

All LEAP centrifuge tests used Ottawa-F65 sand as the soil material. The material characterization of this sand in LEAP among different aspects included extensive assessment of the soil density and hydraulic conductivity. Table 3 summarizes the resulting ranges of the density and hydraulic conductivity, showing the inherent variability of these basic characteristics of the material, as reported by Kutter et al. [4].

Two centrifuge tests NCU-3 [32] and UCD-3 [33] were selected from LEAP-UCD-2017, and three more tests KyU-A1, RPI-A1, and UCD-A2 from LEAP-Asia-2019 [5]. All tests were designed to represent the same prototype of a submerged slope deposit 4 m deep in the middle and 20 m long, with a ground slope of approximately 5°. As these tests were conducted at different centrifuge facilities, the constructed scaled

Table 4
Simulated centrifuge tests in this study.

LEAP	Centrifuge test	Density (kg/m^3)	D_r (%)	PGA_{eff}[a] (g)	CAV_5 (m/s)
UCD-2017	NCU-3	1652	64	0.176	5.84
	UCD-3	1658	67	0.183	7.46
Asia-2019	KyU-A1	1677	73	0.248	11.56
	RPI-A1	1651	64	0.143	7.05
	UCD-A2	1658	67	0.134	5.92

[a] see Kutter et al. [34] for the definition.

models were different in dimensions, depending on the applied centrifugal acceleration. All numerical simulations were carried out at the prototype scale, and therefore the dimensions of the numerical model were the same for all cases.

The initial relative densities of sand deposits were measured before shaking and reported for each centrifuge test. Similarly, the achieved base motions were measured and reported for each test. Table 4 lists a summary of the information related to the achieved soil density and base motion for the five centrifuge tests studied in the paper. The table in particular shows the achieved relative densities in the range of 64–73% for the sand deposits, the effective peak ground acceleration or PGA_{eff} (as defined in Ref. [34]) in the range of 0.134–0.248g, and the cumulative absolute velocity after application of 5 cm/s^2 as threshold acceleration, or CAV_5 in the range 5.84–11.56 m/s, for the applied base motions. Fig. 6 presents the variabilities of the achieved input motion applied at the base of the model container of each centrifuge facility. The response spectra show that in all five tests, the applied motions had a predominant frequency of 1 Hz and different levels of added higher frequency components.

3.2. General numerical platform

The nonlinear finite-difference program Fast Lagrangian Analysis of

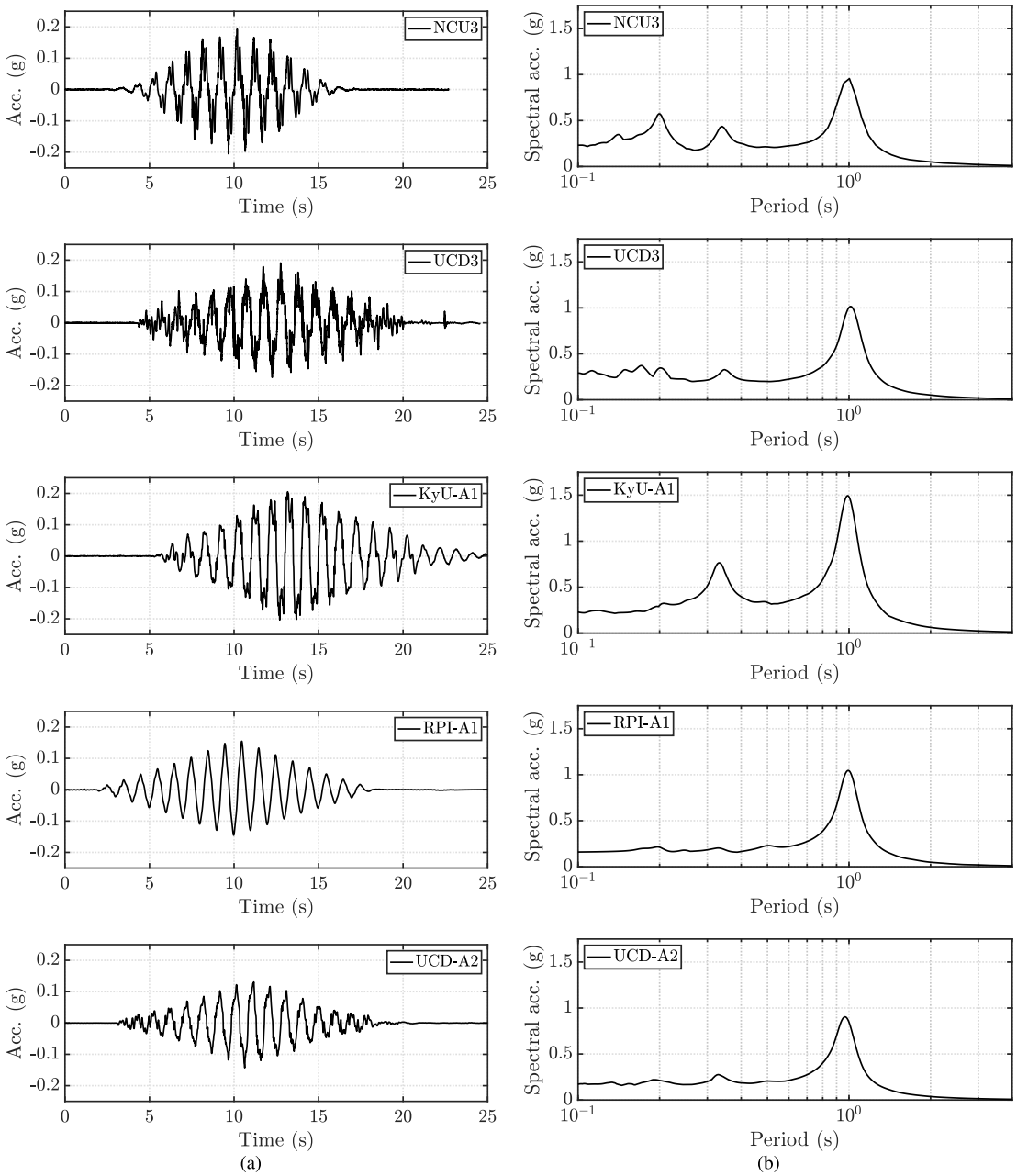

Fig. 6. Achieved input excitations of centrifuge tests in terms of (a) acceleration time history and (b) acceleration response spectra.

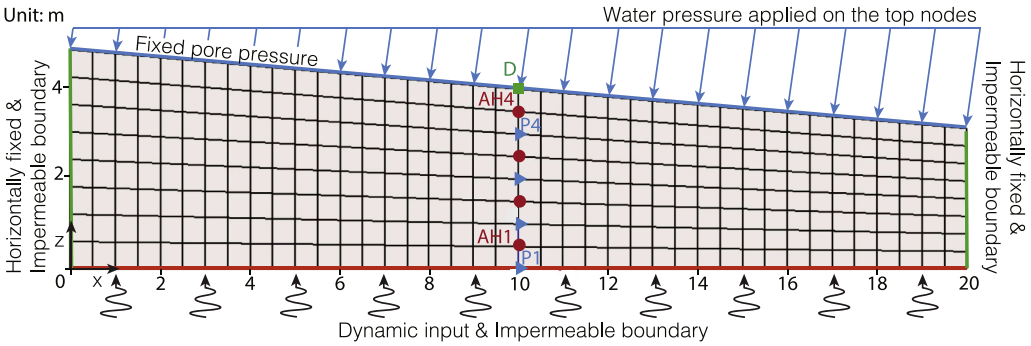

Fig. 7. Two-dimensional view of the FLAC^{3D} mesh showing the boundary conditions, and the recording locations for the selected pore water pressures (P) and horizontal accelerations (AH). The marker for recording the surface displacements (D) was exactly at the center of the model in LEAP-UCD-2017, and close to the centerline in LEAP-Asia-2019.

Continua in three dimensions, or FLAC^{3D} [26], was selected as the main numerical platform. This program solves the full dynamic equation of motion using an explicit time-integration scheme, and includes coupled solid-pore fluid interaction, and large strain formulation making it well suited for solving dynamic stability problems. The simulated medium is represented by brick elements within a 3D grid that are adjusted by the user to fit the target geometry. Each zone (hexahedron) consists of two overlays of five sub-zones (tetrahedron), with a constant strain rate in each sub-zone. This discretization does not generate unwanted hour-glassing modes of deformation. When used in the framework of plasticity, however, these elements do not provide enough modes of deformation; e.g., they cannot deform individually without change of volume. A so-called mixed-discretization process is applied to overcome the overly stiff behavior of uniform strain tetrahedra during plastic flow. Accommodating this process requires special treatments of the internal variables in the integration of elasto-plastic constitutive models, as in the of the SANISAND-Sf model [27].

Two of the relevant analysis configurations that exist in FLAC^{3D} are the fluid-mechanical interaction setting and the dynamic setting. The formulation of coupled deformation-fluid diffusion processes is done within the framework of the quasi-static Biot's theory and can be applied to problems involving single-phase Darcy flow in a porous medium. In the dynamic analysis setting the explicit finite difference scheme of the program is applied to solve the full equations of motion using lumped grid point masses derived from the real density of surrounding zones. The dynamic feature can be coupled with the fluid-mechanical interaction feature, making the software capable of modeling dynamic pore water pressure generation leading to liquefaction in the transient loading process.

3.3. Numerical model description

The prototype scale of the five selected centrifuge tests was set up in the corresponding numerical models in FLAC^{3D} , with the same geometry for all experiments. The model consisted of a three-dimensional mesh with only one zone along the slope strike direction of the slope. The mesh consisted of 40 zones in the slope dip direction, 8 zones in the height direction, and 1 zone in the slope strike direction. The sizes of the zones were 0.5 m in the slope dip direction and 0.39 $\sim$ 0.61 m in the height direction. In total, there are 320 zones and 738 grid points in this model. The spatial discretization of the domain, applied boundary conditions, and locations of the recording sensors/control points are presented in the two-dimensional side view of the model in Fig. 7. The mesh was not allowed to deform in the slope strike direction, and, therefore, worked in the same way as a plane strain condition. The grid points on the model base were constrained in all three directions. The grid points on the side walls were constrained laterally, and the grid points on the top surface were allowed full drainage with fixed values of pore water pressure to model the submerged surface of the slope and replicated the situation in the centrifuge tests.

After establishing the self-weight, the acceleration time histories of the achieved input motions were applied at the base grid points of the model for simulating the dynamic response of the slope, with the details presented in the following section. The symbols AH and P in Fig. 7 refer to the acceleration and pore water pressure control points, respectively. Surface markers around the center of the slope were used to measure displacements. In LEAP-UCD-2017, the surface displacement markers were at the middle center of the models. In LEAP-Asia-2019, however, its location slightly varied from model to model; the markers closest to the centreline were used for the comparisons between experiments and simulations.

3.4. Simulation procedure

The initial stress state in the model was established through a multi-stage numerical approach. First, the slopes with the sand densities in Table 3 were brought to equilibrium under the gravity of 1 g and using a Mohr-Coulomb material model with a bulk modulus of 6.22×10^5 kPa, shear modulus of 2.38×10^6 kPa and a friction angle of 33°. In this process, the mechanical boundary conditions were configured, as shown in Fig. 7, except for the pore water pressure boundary condition on the top surface of the domain. Then, the fluid-mechanical interaction module was activated, and a normal stress gradient representing the target submerged pressures of water was applied on the top surface of the slope, as shown in Fig. 7. Here, the isotropic fluid model was used, with a water bulk modulus of 2.2×10^6 kPa. Soil hydraulic conductivity was first estimated based on the average initial void ratio of the centrifuge tests and the constant head permeability tests conducted by El Ghoraiby et al. [35] (see Table 3) as $k = 1.15 \times 10^{-4}$ m/s. Note that the variation of hydraulic conductivity with the initial void ratios of the centrifuge tests is negligible. In this stage, the pore water pressures at the slope surface were fixed to the corresponding submerged pressures. Upon reaching mechanical and fluid equilibrium, the soil model was switched to SANISAND-Sf. The system with the new model was again brought to equilibrium by continuing the simulation until the changes of stresses and pore water pressures were stabilized.

Fig. 8 depicts contours of initial pore water pressure and state of stresses prior to applying the base excitation for UCD-A2. It can be determined that the initial K_0 values, i.e., the ratio of effective horizontal normal stress σ_{xx} to the effective vertical normal stress σ_{zz}, in each zone, ranged from 0.44 to 0.6, with an average of 0.49. Furthermore, the initial static stress ratios (SSR), i.e., the ratio of offset shear stress τ_{zx} to the effective vertical normal stress σ_{zz}, ranged from 0.01 to 0.06, with an average of 0.04. These ranges and the contour plots for the case of UCD-A2 presented in Fig. 8 are fairly similar to those for the other four centrifuge tests.

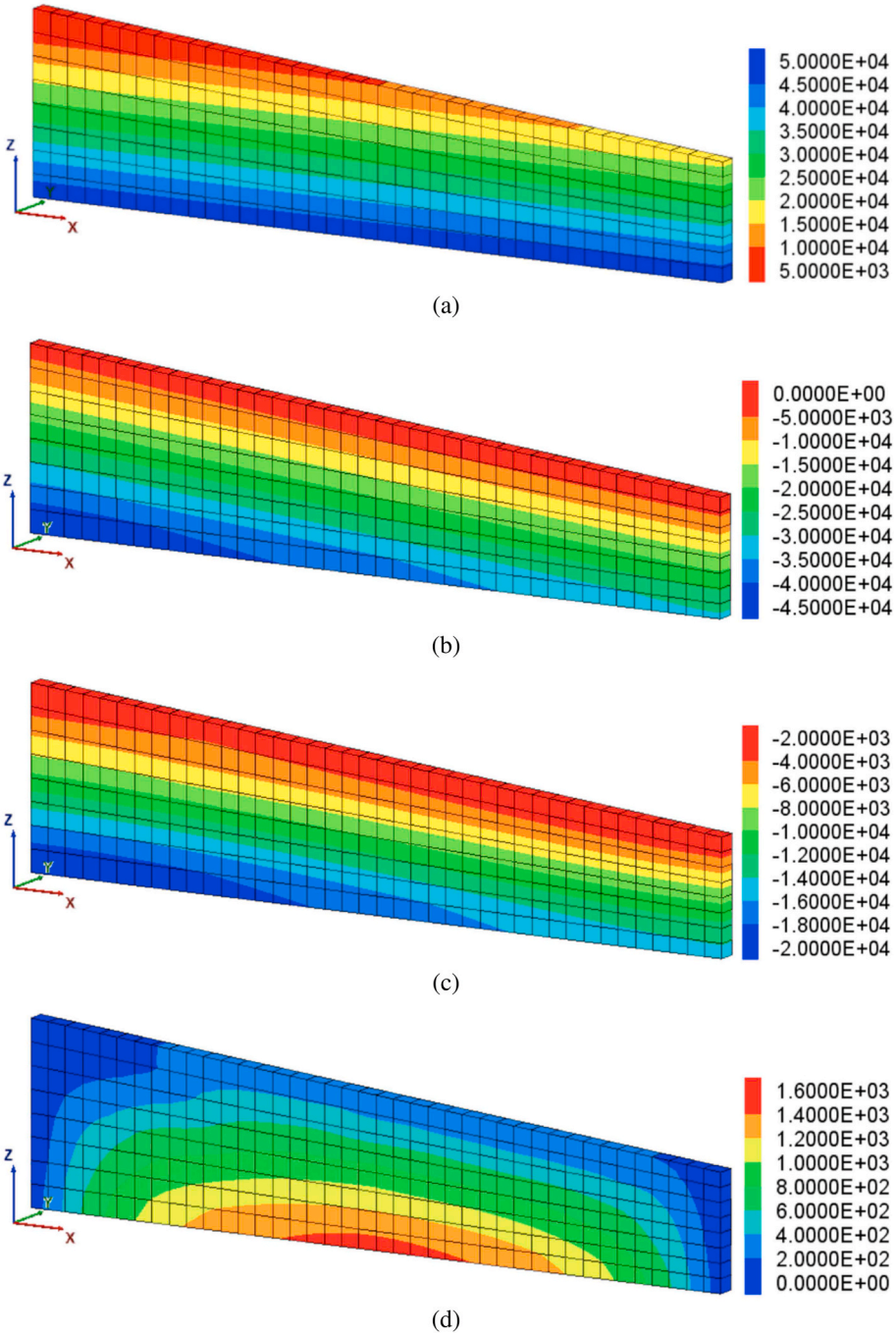

Fig. 8. Contours of initial (a) pore water pressures, (b) effective vertical stresses, (c) effective horizontal stresses, and (d) shear stresses τ_{xz} before shaking for centrifuge model UCD-A2. Units in legends are in Pascals.

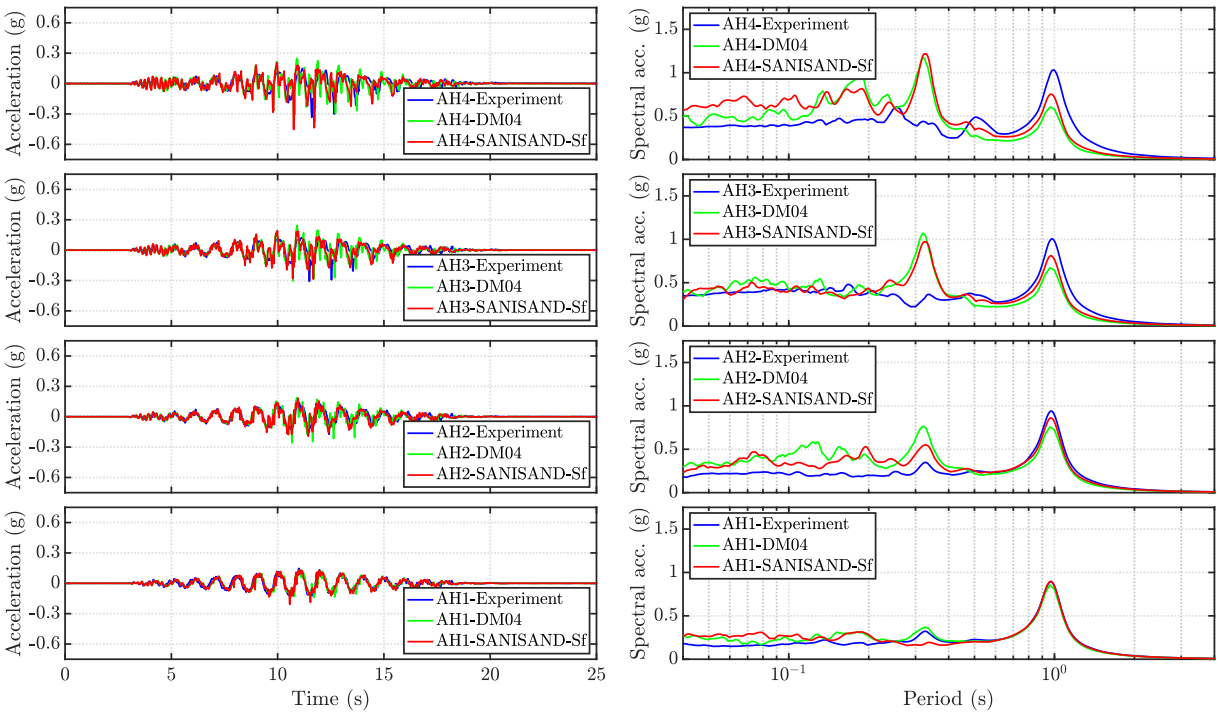

Fig. 9. Experimentally measured and numerically simulated (Class-C) acceleration time histories and response spectra (5% damped) at different control points (AH1–AH4) for UCD-3 centrifuge experiment.

Once the constitutive model was compatible with the initial stress state and the system was in equilibrium, the dynamic analysis feature was utilized, and the corresponding acceleration records were applied at the base grid points in each model. In the dynamic analysis, a Rayleigh damping of 1% with the central frequency of 1 Hz was adopted to reduce the high-frequency numerical noise. Several earlier studies recognized that the hydraulic conductivity k increases at the liquefaction state. Different numerical approaches have been adopted over the years to mimic this elevated level of k [e.g., 36, 37, 7]. In the present study, the hydraulic conductivity was increased to twice the k determined in the laboratory and kept constant during the shaking and dissipating phases to mimic the increase of permeability during the liquefaction stage. This single value is the same as what used in Reyes et al. [8] and provided, on average, the best match to the observed rates of pore water pressure

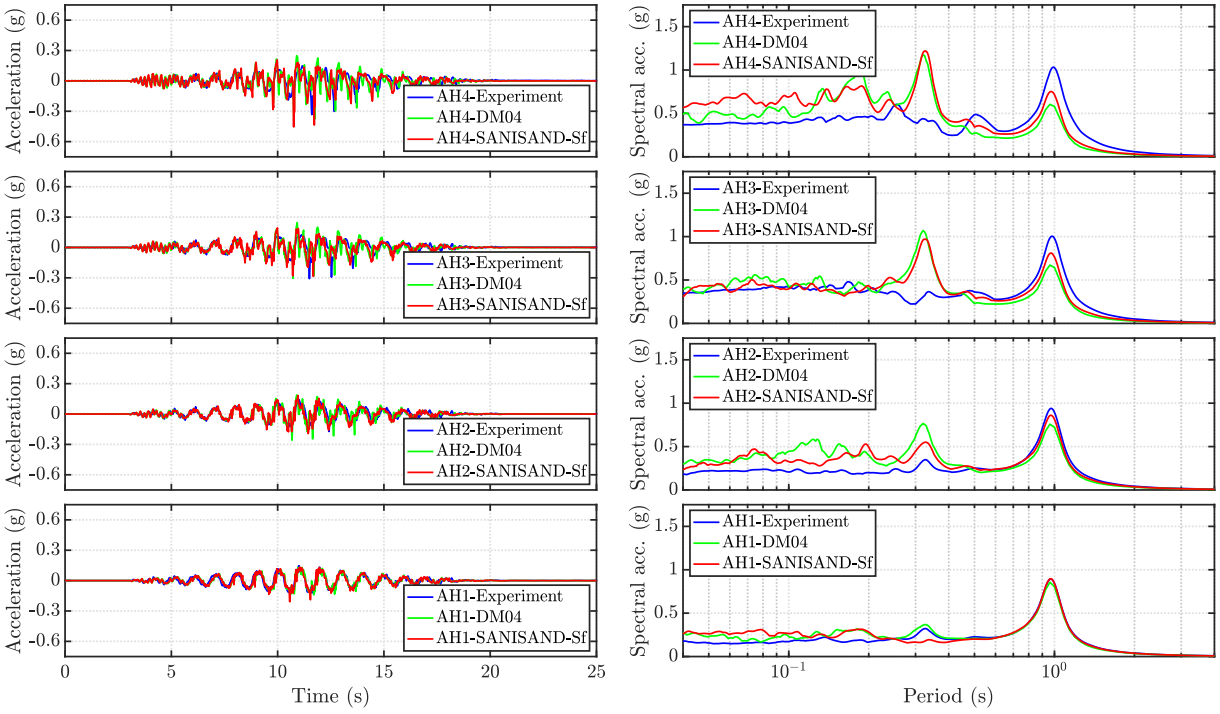

Fig. 10. Experimentally measured and numerically simulated (Class-C) acceleration time histories and response spectra (5% damped) at different control points (AH1–AH4) for UCD-A2 centrifuge experiment.

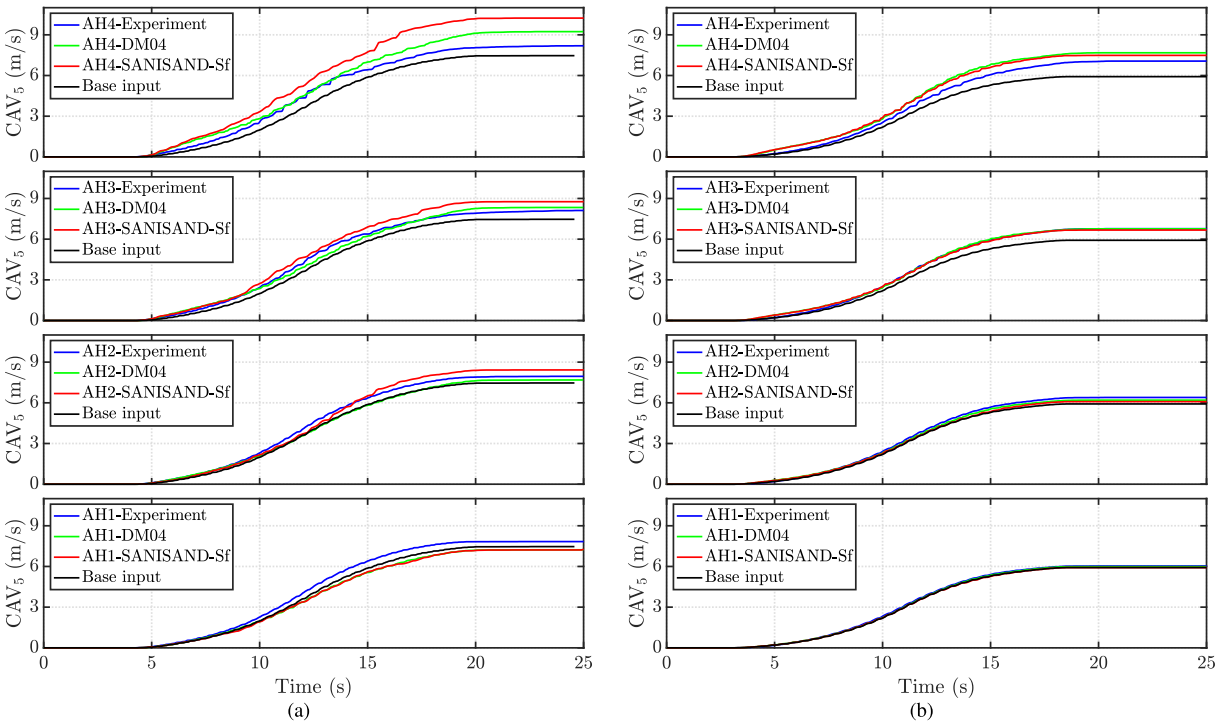

Fig. 11. Experimentally measured and numerically simulated (Class-C) CAV_5 at different control points (AH1–AH4) for (a) UCD-3 and (b) UCD-A2 centrifuge experiments.

dissipation.

3.5. Class-C and Class-C1 simulations

Two sets of numerical simulations, namely, Class-C and Class-C1, were carried out for all five centrifuge tests listed in Table 4, and selected results are presented and discussed. In Class-C simulations, the adopted constitutive model SANISAND-Sf is calibrated against provided laboratory database of element tests, as described in Section 2, and then directly used for simulation of the centrifuge tests. Details of the simulation results, including accelerations, CAV_5, excess pore water pressures, and surface displacements with both reference DM04 and SANISAND-Sf models were compared with the measured ones in the centrifuge tests. Then, for Class-C1, the calibration of the constitutive model was fine-tuned, aiming to achieve a closer match between simulations and experimental results. The performance of the model with the Class-C1 calibration was again assessed in producing the strain-based liquefaction strength curve. Subsequently, Class-C1 simulations were carried out for all centrifuge tests using both DM04 and SANISAND-Sf models.

4. Centrifuge simulation results

4.1. Class-C simulations

Class-C numerical simulations were carried out for all five selected centrifuge tests. The constitutive model constants listed under Class-C in Table 2 were adopted for the reference DM04 and the extended SANISAND-Sf models. Using both constitutive models in the BVP simulations allows assessing the role of the Sf state in a consistent manner as done in the element level simulations in Sec. 2.2. The two sets of simulation results for each centrifuge test were compared with those reported in LEAP at selected control points shown previously in Fig. 7. A detailed assessment of the simulation performance against the experimental measurements is first shown for two of the five tests, i.e., UCD-3 from LEAP-UCD-2017 and UCD-A2 from LEAP-Asia-2019. These two centrifuge experiments were selected as they were conducted in the same centrifuge facility with a similar relative density of sand deposits, thus reducing possible site-to-site variability. The main difference between these two tests was the intensity of their input motion. This detailed comparison of the results includes accelerations, velocities, and excess pore pressures. The same comparisons for the other three tests were checked and found to follow a similar trend, not presented here for the sake of brevity and limited space. However, the measured and simulated horizontal displacements near the center of the slope surface were compared for all the five centrifuge tests, as this aspect of the response is a major focus of the paper.

Figs. 9 and 10 show the experimentally measured and numerically computed (Class-C) acceleration time histories and response spectra (5% damped) at different depths for the UCD-3 and UCD-A2 models. Both simulations show an overall level of agreement with the measured response, but there are some discrepancies. In particular, the numerical simulations underpredict the accelerations at the predominant frequency of the input motion (1 Hz), with the better performance shown by SANISAND-Sf than DM04. The numerical simulations overpredict the accelerations at some higher frequencies, as shown in the response spectra. Ramirez et al. [19] observed that similar high frequencies in their simulations with DM04, and attributed those to the relatively large values of model constants n^b and n^d in Class-C simulations. Smaller values of these constants appeared useful for reducing the high frequencies in the BVP, but at the cost of sight lower predictability of the model when compared to laboratory element tests.

Another intensity measure used for characterizing the motions in dynamic modeling is the cumulative absolute velocity (CAV). In particular, CAV_5, i.e., the CAV with an acceleration threshold of 5 cm/s^2, is an intensity measure that, in some earlier works, was shown to be associated with the liquefaction triggering and excess pore water pressure development in uni- and bi-directional cyclic shearing of soil deposits [21,38]. This association is precisely between the CAV_5 of the base input motion and the excess pore water pressure ratios within level-ground liquefiable deposits. Similar to the approach of examining the acceleration response, it is instructive to also explore the simulations

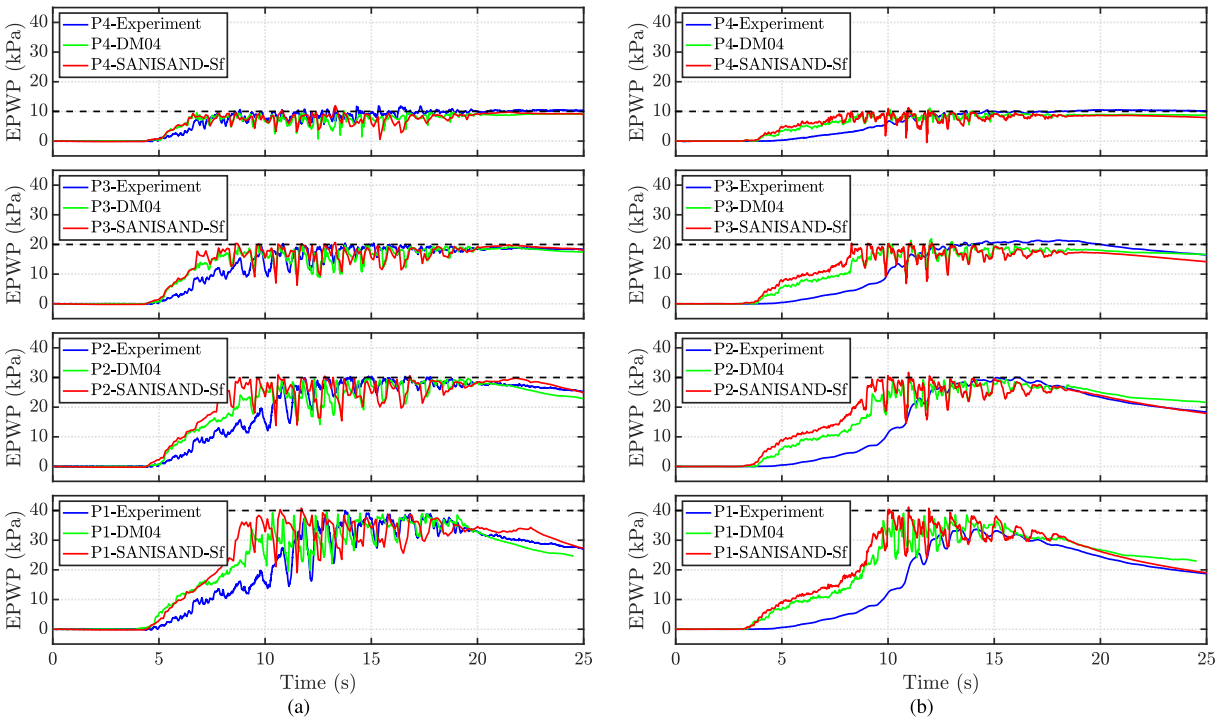

Fig. 12. Experimentally measured and numerically simulated (Class-C) excess pore water pressures at different control points (P1–P4) for (a) UCD-3 and (b) UCD-A2 centrifuge experiments. Dashed lines represent the estimated initial vertical effective stresses.

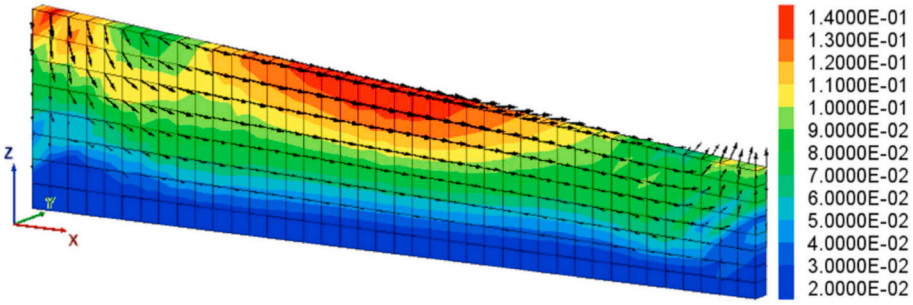

Fig. 13. Vectors and contours of displacements at the end of shaking for the simulation of the UCD-A2 centrifuge test using the SANISAND-Sf model. Units in the legend are in meters.

of this intensity measure at different depths in the soil deposit. Fig. 11 depicts the time histories of CAV_5 at the selected control points. For UCD-3, both DM04 and SANISAND-Sf models overpredict the CAV_5 with slightly better performance by the DM04. For UCD-A2, both models show a reasonable prediction.

Fig. 12 presents the time histories of the excess pore water pressure (EPWP) generation at the selected control points for both UCD-3 and UCD-A2. The SANISAND-Sf model shows very similar results to the reference DM04 model. Both models capture the occurrence of liquefaction, where the EPWP reaches the initial vertical effective stress, but overpredict the generation pace of EPWP at the early stage of shaking. Such overprediction was also observed in previous studies of the authors, and is related to a deficiency of the reference DM04 model in simulating the stress path of undrained cyclic shearing, particularly at low levels of CSR, as happens in the early parts of the base excitation. As this deficiency is related to the response in the pre-liquefaction stage, it is also present in the SANISAND-Sf model. Basically, at small levels of CSR the model tends to underpredict the number of cyclic to reach zero effective stresses or liquefaction. Furthermore, Fig. 12 shows that the models tend to have more dilation spikes compared to the experiments, particularly for UCD-A2. This observation is consistent with the simulated acceleration time histories shown in Fig. 10.

Perhaps the most crucial component of the simulation results is the slope displacements or, more specifically, the surface lateral displacement, as it represents an important engineering demand parameter for a performance-based analysis and design of a sloped deposit. To illustrate the overall displacement response of the simulated sand deposit, Fig. 13 shows the contours of displacements at the end of the base excitation for the centrifuge model UCD-A2 simulated using SANISAND-Sf, along with vectors representing the displacement magnitudes and directions. The shaking appears to have forced an overall rotational movement of the soil mass around the surface center of the model, and a translation of the middle portion parallel to the inclination of the slope.

Fig. 14 shows comparisons of the experimentally measured and numerically simulated surface horizontal displacement time histories at control point D around the center of the slope for all five centrifuge tests

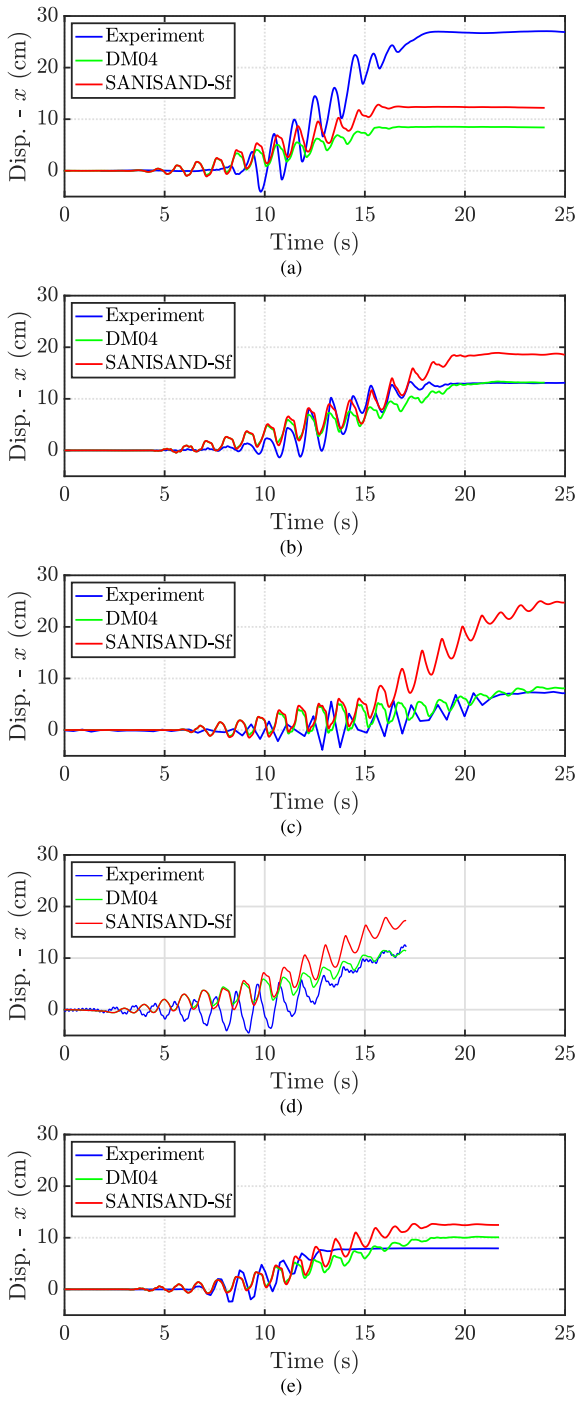

Fig. 14. Experimentally measured and numerically simulated (Class-C) horizontal displacement time histories near the center of the slope surface for the centrifuge models of (a) NCU-3, (b) UCD-3, (c) KyU-A1, (d) RPI-A1, and (e) UCD-A2.

listed in Table 4. Similarly, Fig. 15 presents comparisons of these displacements at the end of shaking, denoted by d_{surf}, for all five tests. Conversely and interestingly, the DM04 results appear to compare, in general, better with the experiments, except for the NCU-3, which underpredicts the d_{surf} by 20 cm. Note that the acceptable performance of the reference model in capturing the lateral surface displacement of the slope is consistent with some other recent studies where DM04 simulations attained good agreements with centrifuge experiments in terms of lateral surface displacement of the slopes [20,39]. It is interesting to observe that while the Class-C calibrated SANISAND-Sf showed

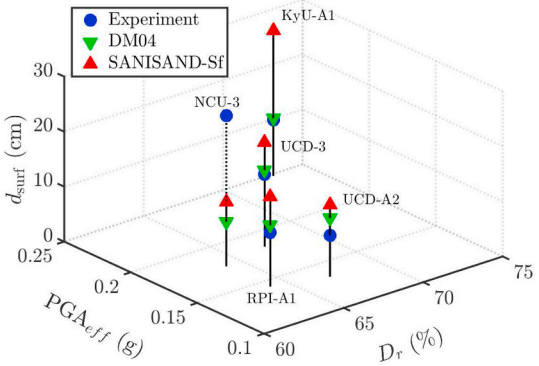

Fig. 15. Comparison of experimentally measured and numerically simulated (Class-C) surface horizontal displacements at the end of the motions, d_{surf} at the control point near the center of the slope surface for all centrifuge models, with respect to their D_r and PGA_{eff} of the base input motions.

superior performance compared to DM04 in capturing the liquefaction strength curves in the element level tests, the latter shows a slightly better performance in capturing the d_{surf}. Recall that in the element level simulations, DM04 showed minimal development of post-liquefaction shear strains because of the locking of the stress-strain loops, as shown in Fig. 4(e). But what could be the reason for these conflicting simulation capabilities?

The overall predictability of the simulations is attributed to a variety of factors. Among the factors that influence the simulated lateral surface displacement of the slope is the choice of the hydraulic conductivity in the simulations. As indicated by Ref. [37], rate of drainage of pore water pressure before the onset of liquefaction, where the generation and drainage of pore water co-occur, is significantly higher than the rate of drainage after ending of liquefaction where the dissipation is the dominant mechanism. This study did not include such a level of detailed treatment of the hydraulic conductivity.

Another important factor is the performance of the constitutive model in the actual loading conditions experienced in the BVP that may be different from those assessed in the model calibration process. In particular, the initial static shear stress present in the centrifuge model sheds some light on this matter. Fig. 16 presents the simulation results of a scenario of undrained cyclic simple shearing on an initial state with a lateral stress coefficient $K_0 = 0.5$ but also with an offset shear stress leading to a static stress ratio SSR $= 0.037$. The model parameters for DM04 and SANISAND-Sf models were taken as those of Ottawa-F65 sand with $D_r = 60\%$. These simulations are configured to approximate cyclic loading history experienced in the BVP of the centrifuge experiments. Compared with the stuck stress-strain loops in Figs. 4(e) and Fig. 16(c) shows that shear strains accumulate in one direction progressively while the width of stress-strain loops is nearly fixed. This ratcheting is because of the static shear stress, which breaks the symmetry of stress-strain loops present in Fig. 4(e) and drives DM04 to develop shear strains along the direction of applied static shear stress. Although no such element level test data is available for Ottawa F-65 sand in the LEAP project, assessing similar tests on other sands in the literature [e.g., 40, 41] reveal that Fig. 16(c) does not match the response in physical testing. For such a low SSR, the stress-strain loops are supposed to extend in both positive and negative shear strains, with more accumulation along the direction of SSR. In other words, the double amplitude of shear strain should continue increasing during the cyclic shearing. In contrast, the DM04 simulation still shows a locked double amplitude of the shear strain. This deficiency has been addressed to a great extent in the SANISAND-Sf, as presented in Fig. 16(f), where stress-strain loops develop in a non-symmetrical pattern, with larger shear strains accumulated along the SSR direction. The Sf state mechanism, however, appears to be generating more shear strains than needed in the presence of offset shear stress. This results in the SANISAND-Sf giving more offset

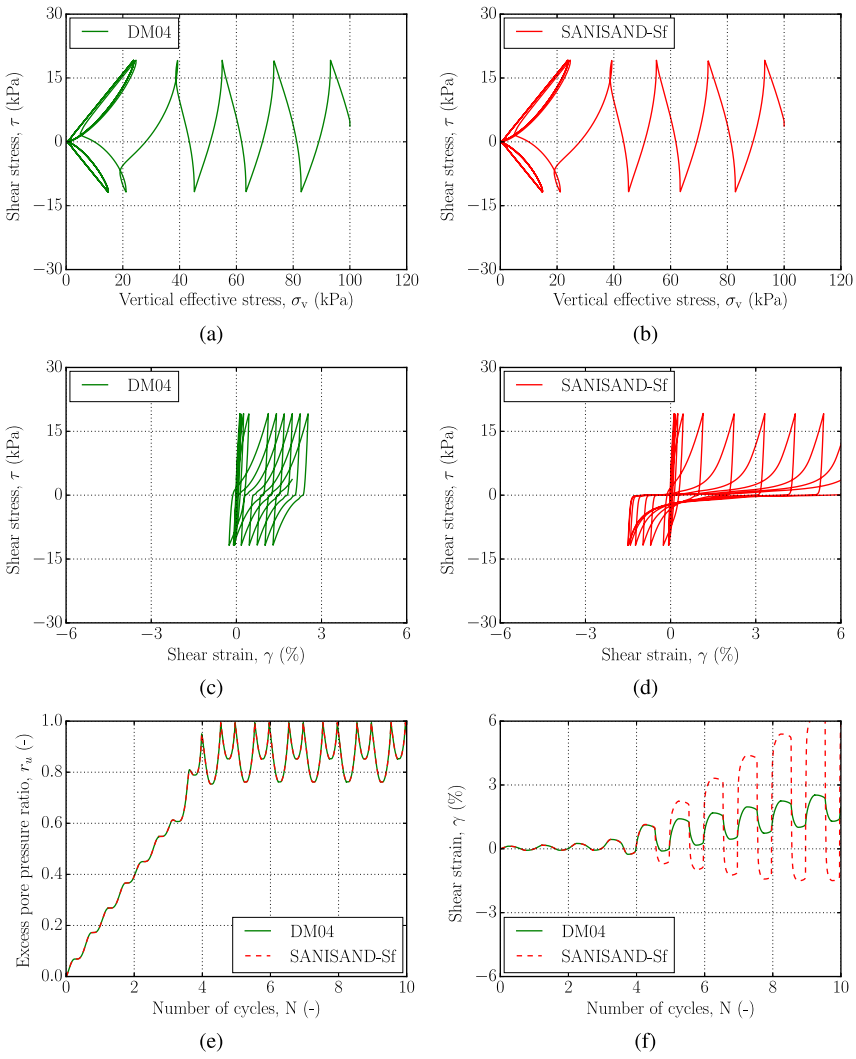

Fig. 16. Simulations of an undrained cyclic torsional loading with CSR = 0.155 on anisotropically consolidated state at D_r = 60%, K_0 = 0.5 and SSR = 0.037, assuming the model constants of Ottawa-F65 sand: (a), (c) simulations using DM04; (b), (d) Class-C simulations using SANISAND-Sf; (e), (f) simulation comparisons between DM04 and SANISAND-Sf in terms of pore water pressure generation and shear strain development.

shear deformation than DM04, which explains the overestimation of lateral surface displacement in Fig. 14. An adjustment in the calibration would be needed to address this overestimation by SANISAND-Sf. In view of these, Class-C1 centrifuge simulations were carried out by adopting a revised set of model constants as described below.

4.2. Class-C1 simulation results

The pieces of evidence shown in the previous section indicate that calibrating the SANISAND-Sf model based solely on cyclic torsional shear tests on isotropically consolidated samples with SSR = 0, as done in Class-C, would lead overestimating semifluidized cyclic shear strains when the cyclic response of the model is assessed in the presence of offset shear stress. It is suggested that cyclic shear straining in the centrifuge simulations, and its resulting lateral displacements, is influenced by the initial K_0 and SSR conditions. Laboratory cyclic simple shear experiments on anisotropically consolidated samples subjected to initial static shear stress would be the optimal basis for calibration of the constitutive model to more accurately simulate the slope problem. Such tests were not available in LEAP during the preparation of this paper. Informed by the model performance in the centrifuge tests, the subsequent Class-C1 calibration of the model was conducted with the philosophy of stiffening the semifluidized response of the constitutive model to indirectly resolve the impact of K_0 and initial static shear stress on post-liquefaction shear strains.

In this Class-C1, SANISAND-Sf was re-calibrated such that in comparison to the Class-C calibration, it now predicts a higher number of cycles in the pre-Sf range and lower number of cycles in the post-Sf range to reach the target γ_{DA} = 7.5%. Without significantly affecting the overall fitting of the CSR-N curve, this approach would lead to smaller development of the semifluidized shear strain in the post-Sf range, which in turn is expected to provide a better estimate of lateral surface displacements in the BVP in the presence of SSR. To achieve this goal, reference model constants n^b and h_0' were increased, and the model constants x and c_ℓ of the Sf state were correspondingly adjusted. The new model parameters were listed in Table 2 under the category of Class-C1. The resulting response in Class-C1 model performance with respect to the hollow cylinder cyclic torsional shear test was slightly compromised when compared to that in Class-C. Fig. 17 presents comparisons between experiments and Class-C1 simulations for a selected undrained hollow cylinder cyclic torsional shear test with CSR = 0.20 in terms of stress-strain loops and stress path. The compromise made for stiffening the model can be primarily observed in the larger number of the simulated cycles in pre-Sf state as shown in the stress paths in Fig. 17 (b) and (c). While the reference DM04 model still shows locking of stress-strain loops (Fig. 17(e)), the changes in the constants x and c_ℓ

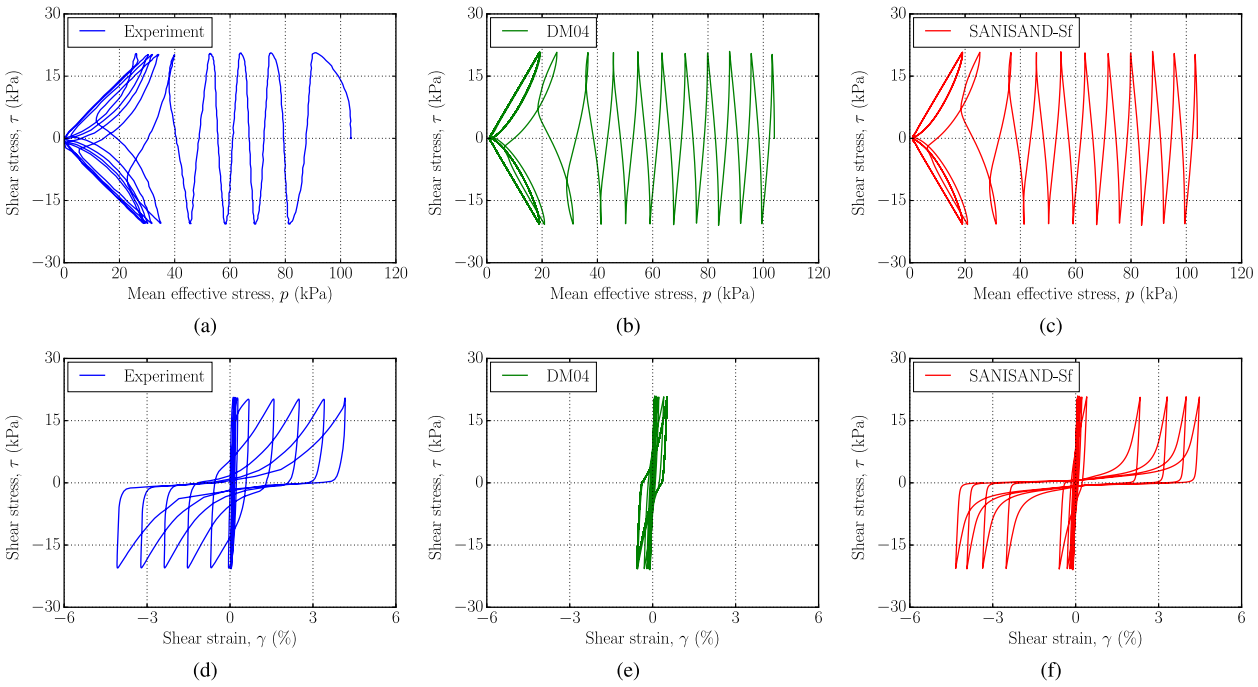

Fig. 17. Updated simulations compared with experiment in undrained hollow cylinder cyclic torsional shear tests with CSR = 0.20 on isotropically consolidated sample of Ottawa-F65 sand with D_r = 60%: (a), (d) experimental data from Vargas et al. [30]; (b), (e) simulations using DM04; (c), (f) Class-C1 simulations using SANISAND-Sf.

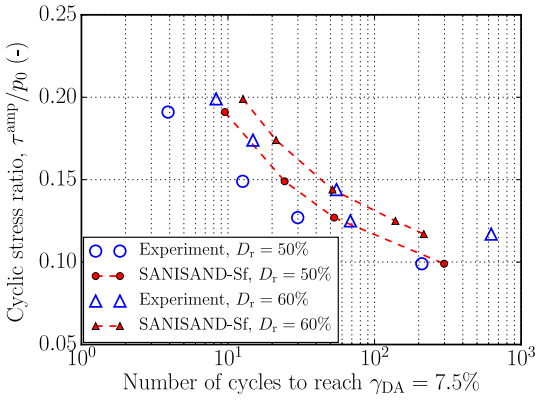

Fig. 18. Experimentally measured and SANISAND-Sf update simulated (Class-C1) liquefaction strength curves to reach γ_{DA} = 7.5% for Ottawa-F65 sand with D_r = 50% and 60%. The corresponding curves from DM04 simulations are again not presented as it did not reach the γ_{DA} = 7.5% criterion at these CSR levels.

allow for the SANISANF-Sf to maintain a reasonable match of shear strain development using the Sf state part, as observed in Fig. 17(f). Fig. 18 shows the liquefaction strength curve for reaching γ_{DA} = 7.5% using the Class-C1 calibration, where the slight compromise of adjusting the model stiffness in the pre- and post-Sf states can be observed mainly at higher levels of CSR.

All five selected centrifuge tests were simulated with the reference DM04 and SANISAND-Sf models and using the Class-C1 model parameters. The overall trend in comparison of the acceleration response, CAV_5 histories, and EPWP evolutions are more or less similar to what was presented in the Class-C predictions of UCD-3 and UCD-A2, and are not repeated here for brevity. Instead, the comparison is only presented for the surface displacements. To this end, consistent with Figs. 14 and 15 in Class-C simulations, Figs. 19 and 20 compare the measured and Class-C1 simulated time histories of surface displacements and the end of shaking d_{surf} for all five centrifuge tests. Except for NCU-3 where the experiment shows a much larger displacement than both models, the new calibration improves the predictability of the SANISAND-Sf model in capturing the lateral surface displacements. In particular, the simulated horizontal displacements at center of the slope match the measured 13 cm for UCD-3 and 7 cm for UCD-A2. The performance of SANISAND-Sf in modeling the surface displacements further confirms its effectiveness in capturing slope lateral displacement for a range of relative densities and input motions. The significantly better match observed in UCD-3, RPI-A1 and UCD-A2 appear to be a consequence of the Class-C1 calibration philosophy, where the stiffer calibrated model led to a slower rate of excess pore water pressure generation in the pre-Sf state, and slower shear strain development in the Sf state, particularly for the experiments with D_r around 60% and sheared under low to medium CSRs.

The DM04 model with the Class-C1 calibration underestimates the surface displacements, as expected, based on the stiffer calibration of the model in the pre-Sf stage. It may be concluded that Class-C1 calibration of SANISAND-Sf finds a balance between the performance at the element level and the centrifuge BVP modeling, and illustrates the capability of the semifluidized constitutive ingredient in simulating the surface displacement of the slope at the end of shaking. While the Class-C calibration of DM04 was also able to capture the surface displacement of the slope in the BVP, the results presented in this section showed the reason behind that success despite the poor performance in capturing the post-liquefaction shear strain development. It is hoped that this comparative presentation of the two models in both element level and BVP illustrates the usefulness of the new semifluidized constitutive ingredient in SANISAND-Sf.

4.3. SANISAND-Sf performance against regression model

The assessment of SANISAND-Sf performance is extended from simulations of five real centrifuge experiments to a sensitivity analysis with respect to varying D_r of the soil deposit and PGA_{eff} of the input motion for a linearly scaled UCD-A2 base motion, and comparing the results with a recently proposed nonlinear regression equation by Kutter

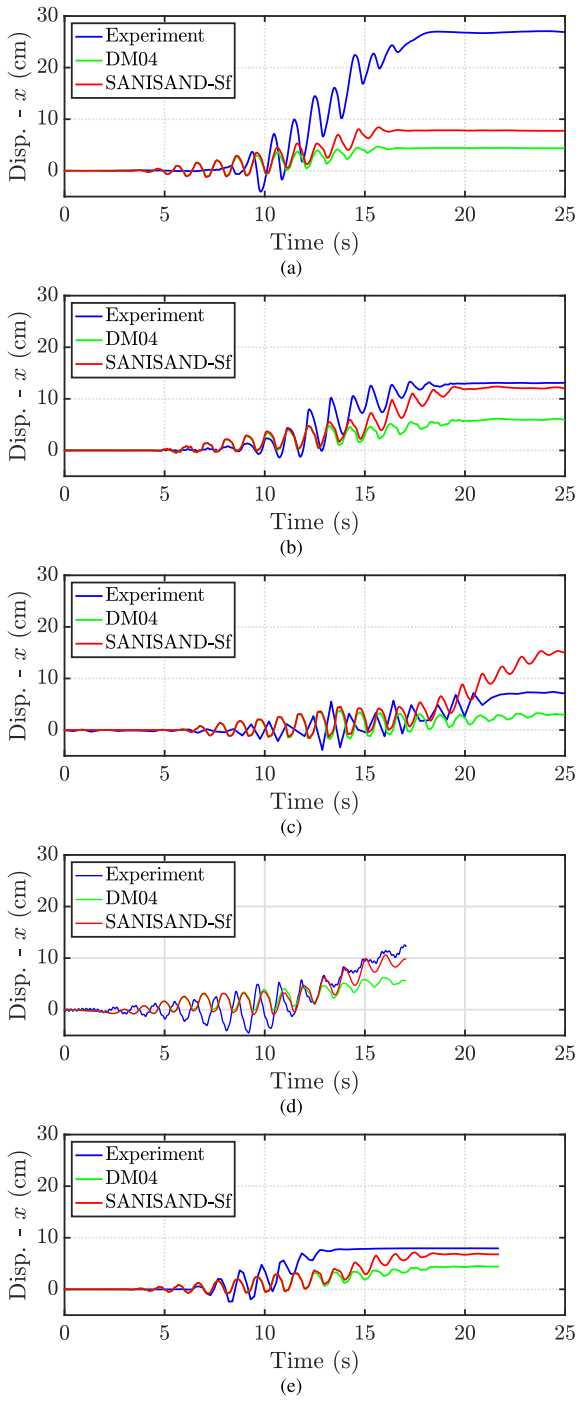

Fig. 19. Experimentally measured and numerically simulated (Class-C1) horizontal displacement time histories near the center of the slope surface for the centrifuge models of (a) NCU-3, (b) UCD-3, (c) KyU-A1, (d) RPI-A1, and (e) UCD-A2.

et al. [42]. This regression model was developed based on a collection of centrifuge experiments of LEAP-UCD-2017 to create a 3D response surface that relates residual surface lateral displacements measured following shaking to initial specimen dry density D_r and PGA_{eff} as an intensity measure of the input motion. The equation of the 3D experimental response surface has the following form

$$d_{surf} = b_2\left\langle b_1 - \frac{(D_r - 0.125)^{n_3} + 0.05}{1.3PGA_{eff}/g}\right\rangle^{n_1} \quad (4)$$

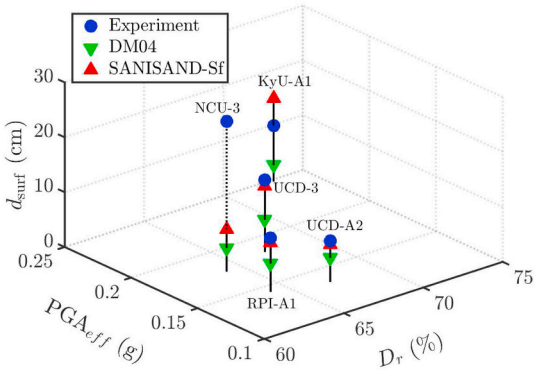

Fig. 20. Comparison of experimentally measured and numerically simulated (Class-C1) horizontal displacements, d_{surf} at the control point near the center of the slope surface for all centrifuge models, with respect to their D_r and PGA_{eff} of the base input motions.

where regression parameters $b_1 = 1.72$, $b_2 = 100$, $n_1 = 4$, and $n_3 = 3.249$ were recommended by Kutter [43], and reported by Carey [44], based on additional data from LEAP-Asia-2019.

Fig. 21(a) shows the 3D surface from the experimental regression model for D_r ranging between 55% and 75% and PGA_{eff} ranging between 0 and 0.3 g. It must be noted that the input motions of centrifuge experiments, which the surface is based on, differ not only in PGA_{eff} but also in frequency content. Also, the correlation coefficient for the nonlinear regression equation varies significantly depending on the form of equation used and the number of experimental data used or excluded as outliers.

For the numerical simulations, several virtual scenarios were analyzed using the Class-C1 calibration of SANISAND-Sf with the D_r varied in the range of 55% and 75%. The analyses were performed using the Incremental Dynamic Analysis (IDA) framework [45] based on linear scaling of the UCD-A2 achieved base motion to cover PGA_{eff} in the range of 0 and 0.3 g. A quadratic best-fit 3D surface was mapped for the simulation results, leading to a correlation coefficient of 0.94. The fitted surface to the numerical simulation results is presented in Fig. 21(b). The difference between the regression model and simulation results is presented in Fig. 21(c).

Generally, SANISAND-Sf captures the effects of D_r and PGA_{eff}, although it appears not to be as sensitive to these quantities as the 3D surface from the experimental regression model. The direct comparison made in Fig. 21 may not be a fair assessment of the success of the numerical model for several reasons. The most obvious one is that the correlation coefficient for the experimental surface was considerably less than 1.0, while it was closer to 1.0 for the numerical surface. Aside from how representative the D_r and PGA_{eff} factors are for estimating the d_{surf}, it must be recognized that the scaled motions used for the numerical simulation had the same frequency content, contrary to the data used for developing the experimental surface. Also, the single set of parameters that were used in the numerical simulations did not have considerations for the uncertainty in the model parameters.

5. Summary and conclusions

This study is focused on assessing the performance of the SANISAND-Sf constitutive model in simulating the experimental of LEAP-UCD-2017 and LEAP-Asia-2019. SANISAND-Sf is an extension of the DM04 model with a recently proposed novel constitutive ingredient for capturing the progressive increase of shear strain amplitudes in the post-liquefaction cyclic shearing of sands. The LEAP element level database on Ottawa-F65 sand was used to calibrate the constitutive model. The performance of the calibrated model was illustrated through modeling of the undrained hollow cylinder cyclic torsional shear tests on isotropically consolidated states of Ottawa-F65 sand. The SANISAND-Sf showed a

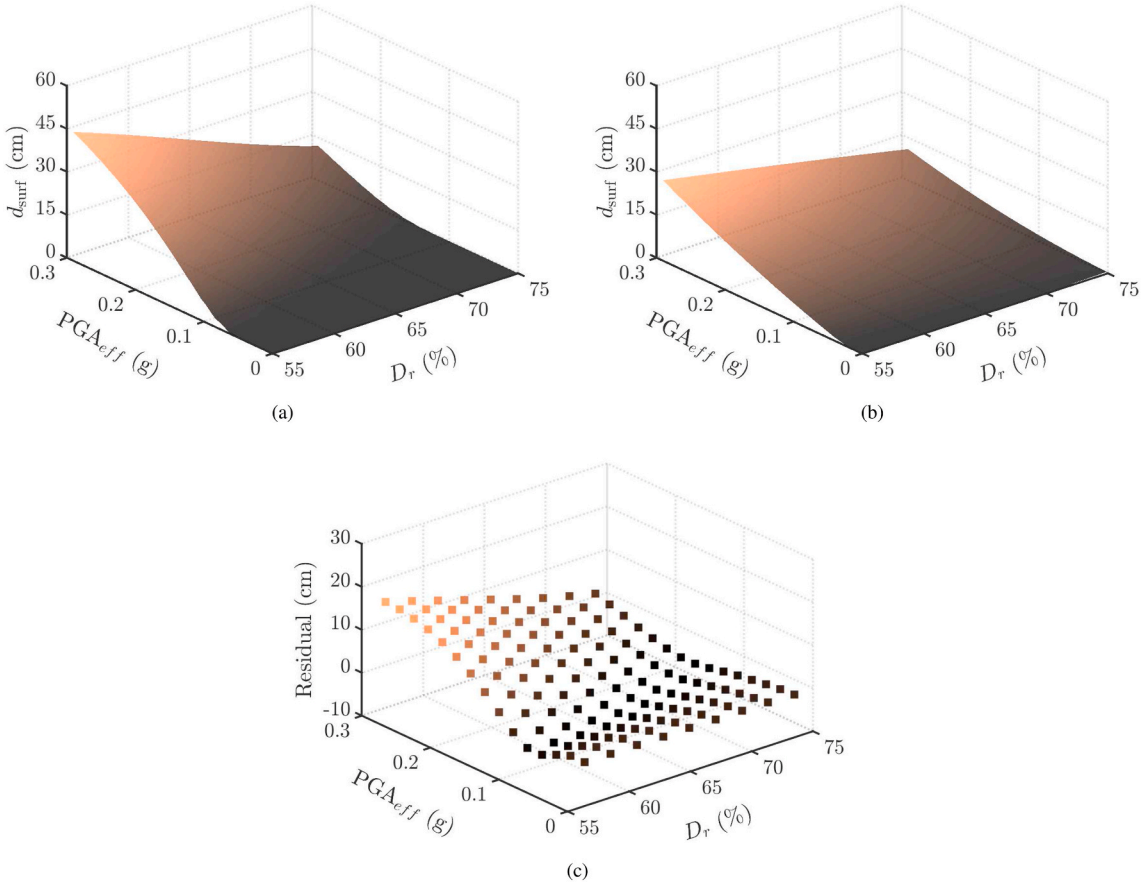

Fig. 21. Comparisons between an experimental regression model and SANISAND-Sf Class-C1 simulations with respect to surface lateral displacements d_{surf} for a range of D_r and PGA_{eff}: (a) 3D surface from the experimental regression model of [42], (b) 3D surface from quadratic fitting to the IDA with UCD-A2 base motion and SANISAND-Sf model, and (c) the difference between (a) and (b).

significantly improved performance over the reference DM04 model in capturing the increasing amplitude of shear strains in the post-liquefaction state and the corresponding strain-based liquefaction strength curve. The DM04 showed locked-up strain amplitudes in the post-liquefaction and was unable to generate enough strains for creating the strain-based liquefaction strength curve. These issues were not present in the SANISAND-Sf simulations.

This so-called Class-C calibration was then used in simulating the prototype scale of five centrifuge experiments on a mildly sloping liquefiable ground of the same soil subjected to dynamic loading from LEAP database. Numerically simulated results using DM04 and SANISAND-Sf were compared with experimentally measured results for acceleration, CAV_5, excess pore water pressure, and displacements. Despite the poor performance of DM04 in the post-liquefaction stage of the element level simulation, compared to the SANISAND-Sf it showed a better prediction of surface displacement at the end of shaking. The reason appeared to be in the Class-C calibration, carried out based on undrained cyclic tests on isotropically consolidated state with no offset shear stress, being too soft for modeling the material response in the presence of initial anisotropy and offset shear stress in the form of static stress ratio, as experienced in the BVP. This aspect was addressed in the Class-C1 stiffer calibration of the model. With this Class-C1 calibration, the SANISAND-Sf still had a lot more realistic performance compared to the DM04 in the element level simulations in capturing the increasing amplitude of shear strains in the post-liquefaction state and the corresponding strain-based liquefaction strength curve. The Class-C1 simulations of the same centrifuge tests resulted in a good estimate of surface displacements using SANISAND-Sf, but under-prediction of those using the reference DM04. These results were consistent with what was observed in the element level simulations. A similar trend was observed in the modeling of the post-shaking slope surface displacements for four of the five simulated centrifuge tests covering a range of relative densities and ground motion intensities. Additional simulations of virtual centrifuge tests covering a range of relative density of soil and PGA_{eff} of the base motion, but only based a linear scaling of one of the centrifuge tests, were contrasted with an experimental regression model for d_{surf} based on a collection of LEAP experiments. The comparison indicates that the SANISAND-Sf with the same set of model parameters provides a reasonable trend of variation of d_{surf} for ranges of PGA_{eff} and D_r. The more significant differences encountered for the lower end of the D_r range and highest values of PGA_{eff}.

The reasons behind some of the disagreements between the numerical simulations and centrifuge experimental measurements are not limited to the constitutive model. Other factors, such as the soil-fluid interaction model and the associated parameters such as hydraulic conductivity and its possible variations during the liquefaction dynamic excitation and liquefaction of the slope deposit, the model boundary conditions, and the base assumptions such as plane-strain condition and the centrifuge scaling laws between the model and prototype scales, can also play important roles. Concerning the constitutive model, it is always safer and more rational to fully validate the various mechanisms of the model that are expected to play a major role in the loading conditions encountered in the BVP. Such rigorous validation steps would lead to more confidence in the prediction capabilities of the model in the complex BVP loading scenarios. The presented simulations and assessments in comparison to the LEAP database show the novel feature of SANISAND-Sf and the adopted numerical modeling approach are effective in capturing the lateral displacements of the centrifuge ex-

periments of mildly sloping liquefiable deposits. The semifluidized state extension of the model for capturing the cyclic shear strains in the post-liquefaction stage of response is certainly a positive step in improving the model. Both DM04 and SANISAND-Sf suffer from the same limitations in terms of accuracy of the pre-liquefaction simulation and other effects. The continual assessments against new laboratory element and centrifuge tests also hint toward additional improvements that are needed in the reference DM04 model. For example, the effect of initial anisotropy and offset shear stress, and also the initial pace of pore water pressure generation in the pre-liquefaction stage of response and particularly in cyclic shearing at low CSR, are areas that require further detailed study. The latter is the subject of the work by Yang et al. [46] that is expected to be used in future projects of LEAP. The cyclic torsional shear tests in LEAP-Asia-2019 were of great value for the evaluation of the post-liquefaction cyclic shear strains. These tests, however, were carried out on isotropically consolidated samples with zero initial static shear stress. The target BVPs, related to the seismic response of sloping ground, have different levels of initial static bias. Therefore, new cyclic torsional shear tests on K_0 consolidated samples and with initial static bias would be beneficial for the calibration stage, and also for the model assessment and likely-needed improvements.

CRediT authorship contribution statement

Andrés Reyes: Conceptualization, Methodology, Software, Validation, Formal analysis, Data curation, Writing - Original Draft, Visualization. **Ming Yang:** Conceptualization, Methodology, Software, Validation, Formal analysis, Data curation, Writing - Original Draft, Visualization. **Andrés R. Barrero:** Conceptualization, Methodology, Software, Validation, Formal analysis, Data curation, Writing - review & editing, Visualization. **Mahdi Taiebat:** Conceptualization, Methodology, Validation, Resources, Writing - review & editing, Supervision, Project administration, Funding acquisition.

Declaration of competing interest

The authors declare that they have no known competing financial interests or personal relationships that could have appeared to influence the work reported in this paper.

Acknowledgements

Support for this study was provided in part by the Natural Sciences and Engineering Research Council of Canada (NSERC). The authors would also like to kindly thank the organizers of LEAP for the insights gained from this collaborative international benchmark study, and Professor Yannis F. Dafalias for the fruitful discussions related to the constitutive modeling component of the research.

References

[1] Arulanandan K, Scott RF, editors. Verification of numerical procedures for the analysis of soil liquefaction problems, A. A. Balkema; 1993.
[2] Manzari MT, Kutter BL, Zeghal M, Iai S, Tobita T, Madabhushi SPG, Haigh SK, Mejia L, Gutierrez DA, Armstrong RJ, Sharp MK, Chen YM, Zhou YG. Leap projects: concept and challenges. In: Iai S, editor. Geotechnics for catastrophic flooding events, taylor & francis group london; 2015. p. 109–16.
[3] Kutter BL, Carey TJ, Hashimoto T, Zeghal M, Abdoun TH, Kokkali P, Madabushi G, Haigh S, dArezzo FB, Madabushi S, Hung WY, Lee CJ, Cheng HC, Iai S, Tobita T, Ashino T, Ren J, Zhou YG, Chen Y, Sun ZB, Manzari MT. LEAP-GWU-2015 experiment specifications, results, and comparisons. Soil Dynam Earthq Eng 2018; 113:616–28.
[4] Kutter BL, Manzari MT, Zeghal M, editors. Model tests and numerical simulations of liquefaction and lateral spreading: LEAP-UCD-2017, springer; 2020.
[5] Tobita T, editor. Model tests and numerical simulations of liquefaction and lateral spreading: LEAP-ASIA-2019; 2020.
[6] Iai S, Tobiota T, Nakahara T. Generalised scaling relations for dynamic centrifuge tests. Geotechnique 2005;55(5):355–62.
[7] Yang M, Barrero AR, Taiebat M. Application of a SANISAND model for numerical simulations of the LEAP 2017 experiments. In: Kutter BL, editor. Model tests and numerical simulations of liquefaction and lateral spreading: LEAP-UCD-2017, springer; 2020. p. 563–78.
[8] Reyes A, Barrero A, Taiebat M. LEAP-ASIA-2019 type-C simulations at the university of British columbia. In: Tobita T, editor. Model tests and numerical simulations of liquefaction and lateral spreading: proceedings of LEAP-ASIA-2019; 2020.
[9] Dafalias YF, Manzari MT. Simple plasticity sand model accounting for fabric change effects. J Eng Mech 2004;130(6):622–34.
[10] Barrero AR, Taiebat M, Dafalias YF. Modeling cyclic shearing of sands in semifluidized state. Int J Numer Anal Methods GeoMech 2020;44(3):371–88.
[11] Manzari MT, Dafalias YF. A critical state two-surface plasticity model for sands. Geotechnique 1997;47(2):255–72.
[12] Taiebat M, Dafalias YF. SANISAND: simple anisotropic sand plasticity model. Int J Numer Anal Methods GeoMech 2008;32(8):915–48.
[13] Dafalias YF, Papadimitriou AG, Li X-S. Sand plasticity model accounting for inherent fabric anisotropy. J Eng Mech 2004;130(11):1319–33.
[14] Dafalias YF, Taiebat M, Sanisand Z. Zero elastic range sand plasticity model. Geotechnique 2016;66(12):999–1013.
[15] Petalas AL, Dafalias YF, Papadimitriou AG, Sanisand-Fn. An evolving fabric-based sand model accounting for stress principal axes rotation. Int J Numer Anal Methods GeoMech 2018;43(1):97–123.
[16] Papadimitriou AG, Chaloulos YK, Dafalias YF. A fabric-based sand plasticity model with reversal surfaces within anisotropic critical state theory. Acta Geotechnica 2019;14(2):253–77.
[17] Petalas AL, Dafalias YF, Papadimitriou AG, Sanisand F. Sand constitutive model with evolving fabric anisotropy. Int J Solid Struct 2019:188–9. 12–31.
[18] Taiebat M, Jeremić B, Dafalias YF, Kaynia AM, Cheng Z. Propagation of seismic waves through liquefied soils. Soil Dynam Earthq Eng 2010;30(4):236–57.
[19] Ramirez J, Barrero AR, Chen L, Dashti S, Ghofrani A, Taiebat M, Arduino P. Site response in a layered liquefiable deposit: evaluation of different numerical tools and methodologies with centrifuge experimental results. J Geotech Geoenviron Eng 2018;144(10):04018073.
[20] Ghofrani A, Arduino P. Prediction of LEAP centrifuge test results using a pressure-dependent bounding surface constitutive model. Soil Dynam Earthq Eng 2018;113: 757–70.
[21] Reyes A, Adinata J, Taiebat M. Impact of bidirectional seismic shearing on the volumetric response of sand deposits. Soil Dynam Earthq Eng 2019;125:105665.
[22] Zhang J-M. Cyclic critical stress state theory of sand with its application to geotechnical problems. Tokyo, Japan: Tokyo Institute of Technology; 1997. Ph.D. thesis.
[23] Wang G, Wei J. Microstructure evolution of granular soils in cyclic mobility and post-liquefaction process. Granul Matter 2016;18(3):51.
[24] Wang R, Fu P, Zhang J-M, Dafalias YF. DEM study of fabric features governing undrained post-liquefaction shear deformation of sand. Acta Geotechnica 2016;11 (6):1321–37.
[25] Barrero AR, Oquendo W, Taiebat M, Lizcano A. Cyclic shearing response of granular material in the semi-fluidized regime. In: Geotechnical earthquake engineering and soil dynamics V, vol. Numerical modeling and soil structure interaction (GSP 292). USA: ASCE; 2018. p. 100–7. Austin, TX,.
[26] Itasca. FLAC3D-Fast Lagrangian analysis of Continua in three-dimensions, version 5.0. Minneapolis, Minnesota: Itasca Consulting Group, Inc.; 2012.
[27] Barrero AR. Multi-scale modeling of the response of granular soils under cyclic shearing. Vancouver, BC, Canada: Department of Civil Engineering, University of British Columbia; 2019. Ph.D. thesis.
[28] Vasko A. An investigation into the behavior of ottawa sand through monotonic and cyclic shear tests, Master's thesis. Washington, USA: The George Washington University; 2015.
[29] Bastidas AMP. Ottawa F-65 sand characterization. Davis, CA, USA: Department of Civil and Environmental Engineering, University of California; 2016. Ph.D. thesis.
[30] Vargas RR, Ueda K, Uemura K. Influence of the relative density and $K_O$effects in the cyclic response of Ottawa F-65 sand - cyclic Torsional Hollow-Cylinder shear tests for LEAP-ASIA-2019. Soil Dynam Earthq Eng 2020;133:106111.
[31] Lambe T. Predictions in soil engineering. Geotechnique 1973;23(2):151–202.
[32] Hung W-Y, Liao T-W. LEAP-UCD-2017 centrifuge tests at NCU. In: Model tests and numerical simulations of liquefaction and lateral spreading, springer; 2020. p. 361–84.
[33] Carey TJ, Stone N, Bonab MH, Kutter BL. LEAP-UCD-2017 centrifuge test at University of California, Davis. In: model tests and numerical simulations of liquefaction and lateral spreading, springer; 2020. p. 255–76.
[34] Kutter BL, Carey TJ, Stone MH, annd Bonab N, Manzari MT, Zeghal M, Escoffier S, Haigh G, annd Madabhushi S, Hung WY, Kim DS, Kim NR, Okamura M, Tobita T, Ueda K, Zhou YG. LEAP-UCD-2017 v. 1.01 model specifications. In: Kutter BLe a, editor. Model tests and numerical simulations of liquefaction and lateral spreading: LEAP-UCD-2017, springer; 2020. p. 41–62.
[35] El Ghoraiby M, Park H, Manzari MT. Physical and mechanical properties of ottawa f65 sand. In: Kutter BL, editor. Model tests and numerical simulations of liquefaction and lateral spreading: LEAP-UCD-2017, springer; 2020. p. 41–62.
[36] Taiebat M, Shahir H, Pak A. Study of pore pressure variation during liquefaction using two constitutive models for sand. Soil Dynam Earthq Eng 2007;27(1):60–72.
[37] Shahir H, Pak A, Taiebat M, Jeremić B. Evaluation of variation of permeability in liquefiable soil under earthquake loading. Comput Geotech 2012;40:74–88.
[38] Kramer SL, Mitchell RA. Ground motion intensity measures for liquefaction hazard evaluation. Earthq Spectra 2006;22(2):413–38.
[39] ElGhoraiby MA, Manzari MT. The effects of base motion variability and soil heterogeneity on lateral spreading of mildly sloping ground. Soil Dynam Earthq Eng 2020;135:106185.

[40] Sriskandakumar S. Cyclic loading response of fraser river sand for validation of numerical models simulating centrifuge tests, Ph.D. thesis, University of British Columbia. 2004.
[41] Chiaro G, Koseki J, Sato T. Effects of initial static shear on liquefaction and large deformation properties of loose saturated Toyoura sand in undrained cyclic torsional shear tests. Soils Found 2012;52(3):498–510.
[42] Kutter BL, Manzari MT, Zeghal M, Arduino P, Barrero A, Carey TJ, Chen L, Elgamal A, Ghofrani A, Montgomery J, Ozutsumi O, Qiu Z, Taiebat M, Tobita T, Travasarou T, Tsiaousi D, Ueda K, Ugalde J, Yang M, Zheng BL, Ziotopoulou K. Numerical sensitivity study compared to trend of experiments for LEAP-UCD-2017. In: Kutter BLe a, editor. Model tests and numerical simulations of liquefaction and lateral spreading: LEAP-UCD-2017, springer; 2020.
[43] B. L. Kutter, Response surface and a few thoughts, Presentation, LEAP-ASIA- 2019 workshop, Osaka, Japan (March 2019).
[44] Carey TJ. Experimental modeling and numerical simulation of lateral spreading for validation of constitutive models. Davis, CA, USA: Department of Civil and Environmental Engineering, University of California; 2019. Ph.D. thesis.
[45] Vamvatsikos D, Cornell CA. Incremental dynamic analysis. Earthq Eng Struct Dynam 2002;31(3):491–514.
[46] Yang M, Taiebat M, Dafalias YF. SANISAND-MSf: a sand plasticity model with memory surface and semifluidised state. Geotechnique 2021. https://doi.org/10.1680/jgeot.19.P.363.